Ocean Color Hyperspectral Remote Sensing With High Resolution and Low Latency—The HYPSO-1 CubeSat Mission

Mariusz E. Grøtte, *Member, IEEE*, Roger Birkeland, *Member, IEEE*, Evelyn Honoré-Livermore, *Graduate Student Member, IEEE*, Sivert Bakken, *Member, IEEE*, Joseph L. Garrett, *Member, IEEE*, Elizabeth F. Prentice, *Member, IEEE*, Fred Sigernes, *Member, IEEE*, Milica Orlandić, *Member, IEEE*, J. Tommy Gravdahl, *Senior Member, IEEE*, and Tor A. Johansen, *Senior Member, IEEE*

***Abstract*— Sporadic ocean color events with characteristic spectra, in particular algal blooms, call for quick delivery of high-resolution remote sensing data for further analysis. Motivated by this, we present the mission design for HYPerspectral Smallsat for Ocean observation (HYPSO-1), a 6U CubeSat at 500 km orbital altitude hosting a custom-built pushbroom hyperspectral imager with wavelengths 387–801 nm at 3.33 nm bandpass and a swath width of 70 km. The imager's expected signal-to-noise ratio is characterized for typical open ocean water-leaving radiance which can be flexibly increased by binning pixels. Using geometric principles, the satellite shall execute a slew maneuver during a scan to induce greater overlap in the pixels with a goal to enable better than 100 m spatial resolution. Since high-dimensional hyperspectral data need to be transmitted over limited space-to-ground communications, we have designed a modular FPGA-based onboard image processing architecture that significantly reduces the data size without losing important spatial-spectral information. We justify the concept with a simulated scenario where HYPSO-1 first collects numerous hyperspectral images of a 40 km by 40 km coastal area in Norway and aims to immediately transfer these to nearby ground stations. Using CCSDS123 lossless compression, it takes about one orbital revolution to obtain the complete data product when considering overhead in satellite bus communications and less than 10 min without the overhead. It is shown that even better latency can be achieved with more advanced onboard processing algorithms.**

***Index Terms*— Hyperspectral imaging, HYPerspectral Smallsat for Ocean observation (HYPSO-1), ocean color, onboard processing, space optics.**

Manuscript received September 17, 2020; revised February 25, 2021; accepted March 22, 2021. This work was supported in part by the Research Council of Norway, Equinor, Det Norske Veritas (DNV), and Sintef through the Centers of Excellence Funding Scheme Grant 223254, Center for Autonomous Marine Operations and Systems (AMOS); in part by the Research Council of Norway through the IKTPLUSS Program Grant 270959, Mission-oriented Autonomous Systems with small Satellites for marItime sensing, surVEillance and communication (MASSIVE) project; in part by the Norwegian Space Agency contract SAT.01.17.7; and in part by the European Research Council on Informatics and Mathematics (ERCIM) postdoctoral fellowship. *(Corresponding author: Mariusz E. Grøtte.)*

Mariusz E. Grøtte, Sivert Bakken, Joseph L. Garrett, Elizabeth F. Prentice, J. Tommy Gravdahl, and Tor A. Johansen are with the Center for Autonomous Marine Operations and Systems (AMOS), Department of Engineering Cybernetics, Norwegian University of Science and Technology (NTNU), 7034 Trondheim, Norway (e-mail: mariusz.eivind.grotte@ntnu.no; sivert.bakken@ntnu.no; joseph.garrett@ntnu.no; elizabeth.prentice@ntnu.no; jan.tommy.gravdahl@ntnu.no; tor.arne.johansen@ntnu.no).

Roger Birkeland, Evelyn Honoré-Livermore, and Milica Orlandić are with the Department of Electronic Systems, Norwegian University of Science and Technology (NTNU), 7491 Trondheim, Norway (e-mail: roger.birkeland@ntnu.no; evelyn.livermore@ntnu.no; milica.orlandic@ntnu.no).

Fred Sigernes is with the University Center in Svalbard (UNIS), 9171 Longyearbyen, Norway, and also with the Center for Autonomous Marine Operations and Systems (AMOS), Department of Engineering Cybernetics, Norwegian University of Science and Technology (NTNU), 7034 Trondheim, Norway (e-mail: fred.sigernes@unis.no).

Digital Object Identifier 10.1109/TGRS.2021.3080175

I. Introduction

HYPERSPECTRAL and multispectral remote sensing are typically utilized in the context of monitoring colorful processes with large spatiotemporal extents. A commonly observed substance is chlorophyll, a light-absorbing pigment involved in phytoplankton photosynthesis which may have clear signatures at the water surface [1]. Blooms of phytoplankton are variable in coloration, often categorized as "red tides," "green tides," or "brown tides" with wavelengths from 400 nm to 700 nm [1]–[6]. They sporadically appear worldwide with varying biomass concentrations, cover regions from tens to hundreds of square kilometers, and may last from a few hours to several days [7]. The malignant ones, often identified as harmful algal blooms (HABs) or cyanobacteria, may cause considerable damage to marine environments, ecosystems, and sustainable food sources such as fish [8]. According to [2], numerous plankton and algae types can be distinguished or inferred from their photosynthetic pigments or fluorescence, where using hyperspectral data with high spectral resolution may reveal subtle spectral inflections imparted by the specific pigment complements. However, the potential harmfulness of algae is not easily determined from optical remote sensing alone and is mostly attributed to *in situ* measurements in the upper water-column [2], [9]. Moreover, challenges in remote sensing also include atmospheric absorption and scattering of light [10], and the fact that the majority of

biomass typically resides between 10 m and 15 m below the water surface [2]. Such heterogeneous and potentially dark targets often demand a combination of larger space-based optics with a high signal-to-noise ratio (SNR), rigorous atmospheric correction schemes, and contemporary *in situ* measurements [11], [12].

Traditional Earth observation (EO) satellites with large optical systems, many of them being operated by the National Aeronautics and Space Administration (NASA) and European Space Agency (ESA), are designed to cover the Earth on a global scale and provide excellent ocean color data with medium-to-high spatial resolution [13], [14], but they normally offer low spectral resolution and revisit times of several days [15]. For example, using multispectral data products from Sentinel-3's Ocean Color and Land Instrument (OLCI) for detecting cyanobacterial blooms based on pigments only, e.g., phycocyanin and chlorophyll-a, can be inaccurate when analyzed by traditional ground-based algorithms, unless employing methods that utilize band ratios from a carefully selected set of spectral bands [16]. Providing greater flexibility in choosing between more than a hundred spectral bands [17], hyperspectral remote sensing missions have shown great promise in ocean color remote sensing, e.g., [18]–[26]. Still, many of these are stand-alone satellite systems that lack the operational flexibility and revisit times to monitor dynamic areas on demand [27]. They also depend on rigorous data processing methods being usually performed on the ground together with careful synergistic analysis of *in situ* measurements, which can be time-consuming before dissemination.

A small satellite, often categorized as nano- or microsatellite, usually has a much shorter lifetime compared to the traditional large satellites but can frequently be replaced with new ones that have up-to-date technology and lower development and production costs [28]. Given the recent advances in sensor technology, miniaturization, and availability of commercial-off-the-shelf (COTS) products, custom-built hyperspectral imagers have now also become suitable for use in nanosatellites [29]–[31]. Instead of mapping on a global scale, such single-purpose hyperspectral imaging nanosatellites may focus on regularly observing smaller dedicated areas to characterize the temporal variation in both spatial and spectral domains, also allowing for smaller camera systems with relatively narrow field of view (FoV). Choosing target area sizes to be at the mesoscale or submesoscale potentially enables small satellites to support a network of *in situ* assets that collect samples or capture images at finer resolution, e.g., unmanned aerial vehicles (UAVs), unmanned surface vehicles (USVs), autonomous underwater vehicles (AUVs), and buoys [8]. To make such a multiagent network work efficiently in real-time and decreasing the operational costs, the remote sensing data must be downloaded quickly to keep the validity in the highly time-varying information.

It is well known that hyperspectral imagers generate a lot of data that consequently take a long time to transfer from space to ground due to limited onboard computational resources, bandwidth, and coverage to ground stations [27], [32]. Reducing data size on board is, therefore, crucial to satisfy real-time requirements but can be difficult given the restricted power available per orbit, especially for small satellites. However, onboard processing has developed considerably for remote sensing in recent years [33], in particular by utilizing reconfigurable Field-Programmable Gate Arrays (FPGAs) that have high computational speed and low power consumption [34], [35]. Enabling algorithm parallelism, an FPGA-based image processing architecture allows modular arrangements of algorithms and processing pipelines. Beyond onboard lossless compression of hyperspectral images, then tailored data products may flexibly contain only the necessary spatial-spectral information extracted from dimensionality reduction, target detection, or classification [36], [37]. The resulting data size reduction grants shorter waiting time between image acquisition to data distribution which can therefore be utilized for real-time applications, e.g., directly supporting algal bloom warning systems [6], [38], [39].

With the goal to provide tailored hyperspectral data products with low latency to support marine environmental monitoring, we present the mission design for the upcoming HYPerspectral Smallsat for Ocean observation (HYPSO-1) developed at the Norwegian University of Science and Technology (NTNU). This article is organized as follows. Section II describes the needs in ocean color remote sensing that motivate the choice of imager design, HYPSO-1's remote sensing capabilities, and the concept of operations (CONOPS). Section III presents the design and performance of the custom-made push-broom hyperspectral imager payload. Section IV describes HYPSO-1's remote sensing technique to enhance the spatial resolution in hyperspectral data by performing a slew maneuver throughout imaging. In Section V we present the HYPSO-1 6U CubeSat, its subsystems, and its power budget for consecutive heavy-duty operations that involve uplink, hyperspectral imaging, onboard processing, and downlink sequences. In Section VI, we describe HYPSO-1's FPGA-based onboard image processing pipelines, provide a survey of potential algorithms for onboard implementation, and justify the mission feasibility regarding the overall latency from image acquisition to data distribution for selected imaging modes and tailored data products. Finally, conclusions are provided in Section VII.

II. Mission Design

A. Objectives

The mission objective for HYPSO-1 is to monitor spatiotemporal extents of biomass and primary production in the ocean using the visual and near-infrared (VIS-NIR) wavelengths from 400 nm to 800 nm, while quickly distributing the data to end-users in near real-time. The key user needs in ocean color remote sensing are:

1) images should have spatial resolution better than 100 m per pixel [15], [40];
2) raw hyperspectral data should have spectral resolution of 5 nm for VIS-NIR wavelengths [15], [40];
3) the SNR at Top of Atmosphere (ToA) should be greater than 400 in visual wavelengths for open ocean water [41], whereas the SNR of atmospherically

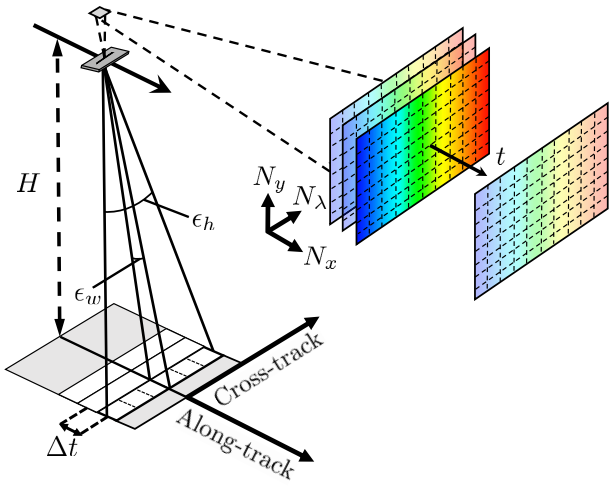

Fig. 1. Illustration of a pushbroom hyperspectral imager collecting N_x frames, or lines, consisting of N_λ and N_y pixels.

corrected water-leaving signals should be between 40–100 [42];
4) data latency should be less than 1 h [43]; and
5) revisit times to dedicated areas of interest should be 3 h–72 h [43], [44].

Because HYPSO-1 is a single nanosatellite, but the first in a prospective constellation, we focus on working toward the recommendations 1), 2), 3) and 4).

B. Image Acquisition Basics

Even though many sorts of spectrometers can be integrated on aerial or space platforms [45], the passive pushbroom imager is an attractive choice that collects a good amount of light [37], [46], [47]. Low-cost COTS components have also made this type more accessible, flexible, and affordable [29], hence chosen as the payload design for HYPSO-1.

A pushbroom imager sequentially scans several lines N_x, each consisting of instantaneous spatial pixels N_y and spectral pixels N_λ, ultimately forming a hyperspectral data cube. Fig. 1 shows the pushbroom imager at altitude H with its scan oriented toward the velocity direction, where N_y pixels are counted perpendicular to the scan direction and N_λ pixels carry the spectral information. The vertical and horizontal FoV components are ϵ_w and ϵ_h, respectively. The integration time $\Delta t = 1/\text{FPS} = \tau + \delta t$ is the elapsed time between two consecutive lines, or frames, where frames per second (FPS) is the frame rate, τ is the camera exposure time and δt is the read-out time.

With the imager mounted in a satellite moving at high orbital speed, the optically induced drawback is generally much lower spatial resolution along the scan direction. A work-around is to overlap more frames by slowly tilting the imager backward as it translates forward, similar to the method described in [48]. This results in a greater amount of partial overlap in the pixels, an effect that can be utilized to enhance SNR or spatial resolution as tradeoffs using image restoration techniques, e.g., deconvolution or super-resolution [49]. For clarity, the Euclidean distance on the ground between the same pixel in two consecutive frames is defined as the Sequential Ground Sampling Distance (SGSD) which is not to be confused with the Ground Sampling Distance (GSD) being the ground distance between adjacent pixels in one instantaneous frame.

C. Concept of Operations

The HYPSO-1 mission is mainly designed based on tradeoffs in spatial resolution, spectral resolution, SNR, data size, coverage to ground stations, and preferred locations to be observed. HYPSO-1 will be launched to a 500 km altitude Sun-Synchronous Orbit (SSO) with Local Time of Descending Node (LTDN) at 10:00 Universal Time Coordinated (UTC), thus granting morning access to the Norwegian coastline during Spring and Summer seasons while also avoiding detrimental sunglint effects [50].

The CONOPS for HYPSO-1, illustrated in Fig. 2, enables five main capabilities:

1) after receiving uploaded telecommands and updates (e.g., camera settings) from a nearby ground station, HYPSO-1 is scheduled to orient its hyperspectral imager to start scanning a predefined region;
2) HYPSO-1 executes a single-axis slew maneuver so that the imager's footprint slowly rotates backward with respect to the velocity direction. With a high camera frame rate, the goal is to enable an SGSD better than 100 m;
3) after imaging, the hyperspectral data cube is immediately processed onboard to reduce its data size and therefore speeding up download on the ground;
4) in the case of quick downlink after observing a coastal region in Norway, the selected ground station network includes S-band ground stations at NTNU in Trondheim, Norway, and Kongsberg Satellite Services (KSAT) in Svalbard, Norway, and Puertollano, Spain; and
5) the Mission Control Center at NTNU Trondheim operates several robotic assets, such as UAVs, USVs, and AUVs, that may collect data *in situ* if within range of the observed area.

D. System Capabilities

1) Imaging Modes: The hyperspectral imager has three main configurations for image acquisition:

1) high-resolution mode: enables high spatial resolution with narrow swath width and high frame rate settings;
2) wide FoV mode: enables a wider swath but at coarser spatial resolution; and
3) diagnostics mode: provides raw data at full sensor resolution mainly to be used for in-orbit calibration and characterization.

2) Attitude Determination & Control System: To obtain better than 100 m spatial resolution requires a precise attitude determination and control system (ADCS) [30]. For a pointing or maneuvering satellite, attitude sensor and actuator noise (e.g., reaction wheel jittering) will result in a nonuniform distribution of images across the observed scene. The attitude inaccuracies can be categorized by attitude control and knowledge errors, bearing in mind that the latter affects the former.

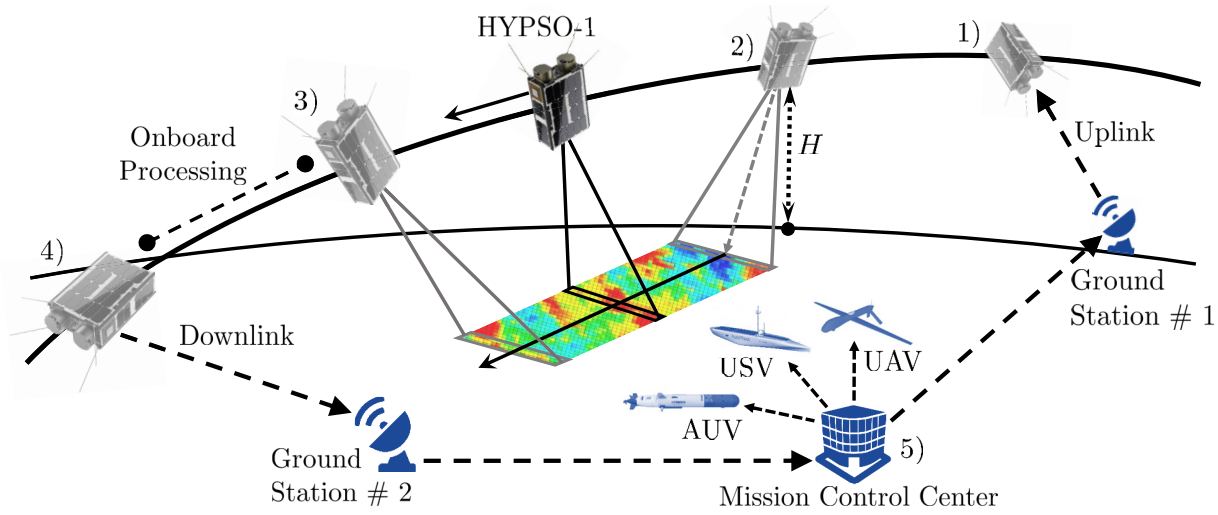

Fig. 2. CONOPS for HYPSO-1 where it 1) receives uploads from a nearby ground station; 2) acquires hyperspectral images during a slew maneuver; 3) immediately processes the images on board; 4) downlinks the data to nearby ground stations; and 5) supports *in situ* assets in the vicinity that may be deployed to the observed scene for closer investigation.

To achieve consistent image registration or simply knowing the location of each pixel to the accuracy of 100 m, e.g., for georeferencing, then good performance is needed for attitude and position determination and time synchronization between the images, attitude data, and position data.

3) Onboard Image Processing: The image processing architecture shall be modular by design, alleviate the satellite operations, and quickly provide tailored data upon requests from end-users. To make such data products useful, the high-level goals are to:

1) employ lossless compression on hyperspectral data to reduce their size on board for quicker download;
2) extract relevant spatial-spectral information in the water-leaving signals by using e.g., dimensionality reduction, target detection or classification;
3) register and rectify the images, and utilize the SGSD to achieve better than 100 m spatial resolution by using image restoration methods, e.g., deconvolution or super-resolution; and
4) be able to transform pixel indices to geodetic latitude and longitude, e.g., using georeferencing, such that the coordinates may guide *in situ* assets to specific locations of interest.

The hyperspectral data products shall normally be analyzed in synergy with other available remote sensing data and *in situ* measurements, especially during HYPSO-1's commissioning phase. In addition, modeling and simulation tools shall provide estimated radiometric, spectral, and spatial properties of a simulated ocean color event to support data analysis and atmospheric correction [51], [52].

III. Hyperspectral Imager Design

A. Optics

An optical diagram of HYPSO-1's pushbroom hyperspectral imager is shown in Fig. 3 with its cross section parallel to the refraction axis [37]. The components are: 1) a front lens with aperture diameter D_0 and focal length F_0; 2) an entrance slit with height h_{slit} and width w_{slit}; 3) a collimator lens with aperture diameter D_1 and focal length F_1; 4) a grating receiving the incoming light at angle $\alpha = 0°$ then diffracting it at angle β with respect to the grating normal; 5) a detector lens with aperture diameter D_2 and focal length F_2; and finally 6) an image sensor. The FoV components along and perpendicular to the scan direction are

$$\tan\left(\frac{\epsilon_w}{2}\right) = \frac{w_{\text{slit}}}{2F_0} \tag{1a}$$

$$\tan\left(\frac{\epsilon_h}{2}\right) = \frac{h_{\text{slit}}}{2F_0}. \tag{1b}$$

Assuming no loss in light transmission from the front lens to the image sensor, the geometric etendue can expressed as

$$G = \pi \frac{D_0^2}{4F_0^2} \cos(\beta) w_d h_d \tag{2}$$

where the projection of the slit dimensions onto the image sensor are

$$w_d = \frac{w_{\text{slit}} F_2}{\cos(\beta) F_1} \tag{3a}$$

$$h_d = h_{\text{slit}} \frac{F_2}{F_1} \tag{3b}$$

and β is the diffraction angle assumed at the center wavelength [53]. Shown to the right in Fig. 3, the number of illuminated pixels along the projected slit width and height are

$$N_w = \frac{w_d}{\Delta p_\lambda} \tag{4a}$$

$$N_h = \frac{h_d}{\Delta p_y} \tag{4b}$$

where Δp_λ and Δp_y are the pixel width and height, respectively.

The theoretical spectral bandpass for the optical system is the recorded full width at half maximum (FWHM) of

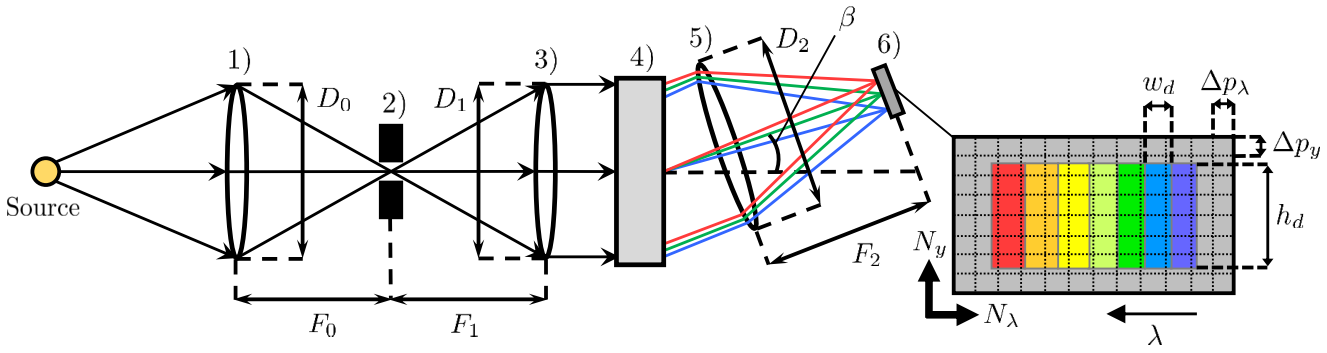

Fig. 3. Schematic of the grating-type pushbroom hyperspectral imager. Light is first focused into a slit, collimated into a grating which then diffracts the light to an image sensor. Shown to the right, the projected slit onto the image sensor plane with effective width w_d and height h_d corresponds to one spectral band. The camera's mechanical layout may block some of the light as indicated by gray pixels and weaker signals can be expected in pixels at the edges because of partial illumination.

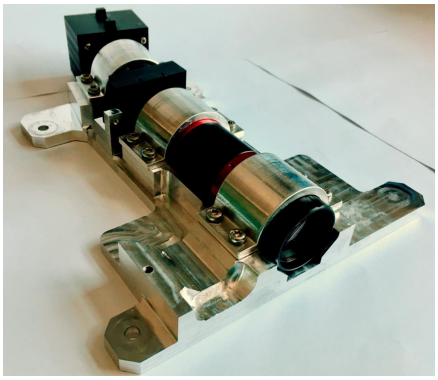

Fig. 4. Hyperspectral imager payload assembled for integration into HYPSO-1.

a monochromatic spectral line and indicates how well the adjacent spectral bands are resolved. Assuming no degradation due to aberrations and diffraction, the spectral bandpass may be approximated as

$$\Delta\lambda \approx \frac{g\, w_{\text{slit}}}{\kappa\, F_1} \tag{5}$$

where g is the groove spacing of the grating and κ is the spectral order [53].

B. Payload Flight Model

HYPSO-1's hyperspectral imager, shown in Fig. 4, is designed to provide a spectral range from 400 nm to 800 nm at a bandpass of 3.33 nm and is mainly built using COTS components from Thorlabs and Edmund Optics along with a few custom machined parts. The F-numbers of the lenses are here set as $F_0/\# = F_1/\# = 2.8$ and $F_2/\# = 2$ to avoid detrimental stray light effects, even though in theory they should be equal to maximize the light throughput.

A SONY IMX249 image sensor is mounted in an industrial camera head from Imaging Development Systems (IDS) GmbH. It has 1936×1216 pixels with a reported well depth of about 33 022 e^- (electrons) per pixel, equivalent to maximum SNR of approximately 181.6. The camera's upper limit on frame rate is FPS $=$ 47 but in practice, this can be lower depending on the data throughput and the chosen number of binning operations, subsampling, bit-depth, and area of interest (AoI), where the latter is the selected number of pixels in a custom image sensor window. For more details, the key specifications of the payload instrument are given in Table I.

TABLE I
HYPERSPECTRAL IMAGER SPECIFICATIONS

Parameter	Value
Volume	200 mm × 65 mm × 65 mm
Mass	1.6 kg
FoV $\epsilon_w \times \epsilon_h$	0.0564° × 7.8826°
Focal length $F_0 = F_1 = F_2$	50 mm
F-number $F_0/\# = F_1/\#$	2.8
F-number $F_2/\#$	2
Diameter $D_0 = D_1$	17.9 mm
Diameter D_2	25 mm
Slit width w_{slit}	50 μm
Slit height h_{slit}	7 mm
Optical efficiency $\eta_0 = \eta_1 = \eta_2$	0.8
Grating efficiency η_G @500 nm	0.73
Spectral order κ	1
Groove spacing g	3 333.33 nm
Diffraction angle β	10.37°
Pixel size $\Delta p_\lambda = \Delta p_y$	5.86 μm
Usable sensor resolution	1 936 × 1 194 pixels
Quantum efficiency η_Q @500 nm	0.77
Full spectral range (calibrated)	200–967 nm
Spectral bands at full resolution	at least 215
Theoretical bandpass $\Delta\lambda$	3.33 nm
Dark current i_{dark}	0.95 e^-/s
Read-out noise $C_{\text{read-out}}$	6.93 e^-
Quantization noise C_{quant}	2.33 e^-
Max. SNR per pixel (not binned)	181.6 (45.2 dB)
ADC bit-depth	12 b (bits)

C. Characterizing the SNR

Obtaining high SNR in hyperspectral imagery improves the accuracy in discriminating dimmer optical constituents in water scenes which is important for in-orbit calibration, atmospheric correction, and feature extraction in image processing. Starting with the total ToA radiance reaching the imager's front lens, it is comprised of several components that are functions of wavelength and viewing direction [54], [55]

$$L_{\text{tot}}^{\text{ToA}} = L_{\text{atm}}^{\text{ToA}} + t_{\text{dir}} L_{\text{sg}} + t_{\text{diff}} L_{\text{wc}} + t_{\text{diff}} L_{\text{water}} \tag{6}$$

where $L_{\text{atm}}^{\text{ToA}}(\lambda)$ is the combined radiance due to Rayleigh, aerosol, Rayleigh-aerosol interaction, and sky background, and $L_{\text{sg}}(\lambda)$, $L_{\text{wc}}(\lambda)$ and $L_{\text{water}}(\lambda)$ are the sun glint radiance, sun and sky radiance reflected by whitecaps and foam, and water-leaving radiance, respectively. The terms $t_{\text{dir}}(\lambda, \gamma; H)$ and $t_{\text{diff}}(\lambda, \gamma; H)$ are the direct and diffuse transmittances along the imager's optical path that are governed by wavelength λ, viewing angle γ, and altitude above the surface H.

Writing $L_{\text{ref}}^{\text{ToA}}(\lambda)$ as an arbitrary reference signal to be detected at ToA, it can therefore be a chosen term of interest from (6), for example, the total ToA radiance $L_{\text{ref}}^{\text{ToA}}(\lambda) = L_{\text{tot}}^{\text{ToA}}(\lambda)$ or a component therein, e.g., the water-leaving radiance $L_{\text{ref}}^{\text{ToA}}(\lambda) = L_{\text{water}}^{\text{ToA}}(\lambda)$. The photon flux reaching the sensor per spectral bandpass is then

$$\dot{\Phi}_{\text{ref}}^{\text{ToA}} = L_{\text{ref}}^{\text{ToA}} \eta_0 \eta_1 \eta_G \eta_2 G \lambda \frac{\Delta\lambda}{h_{\text{planck}} c} \tag{7}$$

where $L_{\text{ref}}^{\text{ToA}}(\lambda)$ is the reference radiance, η_0, η_1, η_2 are the optical efficiencies of the front, collimator, and detector lenses, respectively, $\eta_G(\lambda)$ is the grating efficiency, c is the speed of light, and $h_{\text{planck}} = 6.62607015 \times 10^{-34}$ J $\cdot$ s is Planck's constant. The count of photon-electrons per pixel is therefore

$$C_{\text{ref}} = \frac{\eta_{\text{Q}} \dot{\Phi}_{\text{ref}}^{\text{ToA}} \tau}{N_w N_h} \tag{8}$$

where $\eta_{\text{Q}}(\lambda)$ is the quantum efficiency of the image sensor. In general form, the SNR for a reference ToA signal in one pixel, i.e., a [1, 1] window, can be expressed as

$$\text{SNR}_{\text{ref},[1,1]} = \frac{C_{\text{ref}}}{\sqrt{C_{\text{ref}} + C_{\text{dark}} + C_{\text{read-out}}^2 + C_{\text{quant}}^2}} \tag{9}$$

where C_{ref} and C_{dark} have Poisson probability distributions, and $C_{\text{read-out}}$ and C_{quant} have Gaussian probability distributions with zero mean [56], [57]. The average shot noise registered due to the sensor's dark current i_{dark} is $C_{\text{dark}} = i_{\text{dark}} \Delta t$, $C_{\text{read-out}}$ is the standard deviation of electrons in the sensor read-out circuits, and $C_{\text{quant}} = C_{\max}/(2^{\text{bit-depth}}\sqrt{12})$ is the standard deviation of quantization noise where $C_{\max}$ is the well-depth and bit-depth is that of the analog–digital converter (ADC).

1) Binning: With the ability to bin pixels on the image sensor, photon-electrons can be gathered from adjacent pixels to create a merged pixel resulting in the signal being increased proportionally with the square root of a number of binning operations. To increase the SNR without losing spectral resolution, one may therefore fully bin $B_\lambda = \lceil N_w \rceil$ pixels that approximately contain one spectral bandpass, where B_λ is the number of binning operations in the spectral dimension and $\lceil \cdot \rceil$ indicates rounding up a value to the nearest integer. This results in an effective SNR of $\text{SNR}_{\text{ref},[\lceil N_w \rceil,1]} \approx \sqrt{N_w} SNR_{\text{ref},[1,1]}$. Similarly, binning B_y instantaneous spatial pixels along h_d also results in higher SNR but then at the cost of spatial resolution.

2) SNR for Total ToA Radiance: Earth's atmosphere reflects a lot of sunlight and significantly distorts visible light traveling from the surface until reaching space, such that the actual water-leaving radiance L_{water} may constitute a mere 10% of the total ToA radiance $L_{\text{tot}}^{\text{ToA}}$ [58], [59]. $L_{\text{tot}}^{\text{ToA}}$ for open ocean water scenes can typically range from 0.005 W/(m^2 $\cdot$ sr $\cdot$ nm) to 0.06 W/(m^2 $\cdot$ sr $\cdot$ nm) at wavelengths 400–800 nm with the strongest signals being in blue-green and decreasing toward the red part of the spectrum [60]. Assuming $L_{\text{tot}}^{\text{ToA}} = 0.042$ W/(m^2 $\cdot$ sr $\cdot$ nm) based on [60] and setting $\tau = 51.6$ ms, our hyperspectral imager would get $\text{SNR}_{\text{total},[1,1]} \approx 133$ and $\text{SNR}_{\text{total},[9,1]} \approx 392$ for $B_\lambda = 9$, whereas $B_\lambda = 18$ gives $\text{SNR}_{\text{total},[18,1]} \approx 554$ but at the cost of spectral resolution worsening from $\Delta\lambda = 3.33$ nm to $\Delta\lambda = 6.67$ nm. Noteworthy, a radiance of $L_{\text{tot}}^{\text{ToA}} = 0.0725$ W/(m^2 $\cdot$ sr $\cdot$ nm) results in $\text{SNR}_{\text{total},[1,1]} \approx 182$ which is above the saturation capacity for the SONY IMX249 at SNR of 181.6. If raw pixels are expected to saturate at wavelengths of interest, then one could appropriately decrease the camera exposure time τ or increase the saturation capacity by binning more pixels.

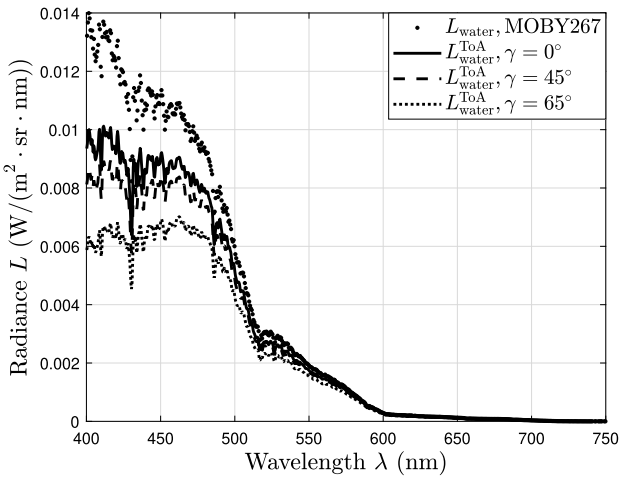

Fig. 5. Water-leaving radiance L_{water} measured by MOBY number 267 and estimated water-leaving radiance at ToA $L_{\text{water}}^{\text{ToA}}$, for viewing angles $\gamma = 0°$, 45°, and 65°.

3) SNR for Open Ocean Water: To estimate the imager's ability to recognize the target radiance $L_{\text{water}}^{\text{ToA}}$, we have used publicly available and calibrated water-leaving radiance measurements from the Marine Optical BuoY (MOBY) deployment number 267 off the coast of Hawaii [61], being time-stamped at 21:11:38 UTC 3 July 2019. This particular day has a typical radiance profile for open ocean water, hence a good example for a scene to be observed by HYPSO-1 even though the signals are weak in the red part of the spectrum. Fig. 5 shows the MOBY measurements of the water-leaving radiance at the surface $L_{\text{water}}(\lambda)$, and the simulated water-leaving radiance at ToA $L_{\text{water}}^{\text{ToA}}(\lambda) = t_{\text{diff}}(\lambda, \gamma, H) L_{\text{water}}(\lambda)$. The original MOBY measurements are fit with a spline curve to match the 3.33 nm bandpass of the hyperspectral imager in the wavelength range 400–750 nm. Furthermore, the water-leaving signals traveling to ToA are assumed to be weakened by only the Rayleigh optical thickness based on [62]. This assumption does not include other transmittance models and distortions due to atmospheric effects that partially govern $L_{\text{tot}}^{\text{ToA}}$, e.g., Rayleigh scattering, aerosol scattering, Rayleigh-aerosol interactions and sun reflection [58]. A more realistic atmosphere can be modeled for complete details but is considered to be beyond the scope here.

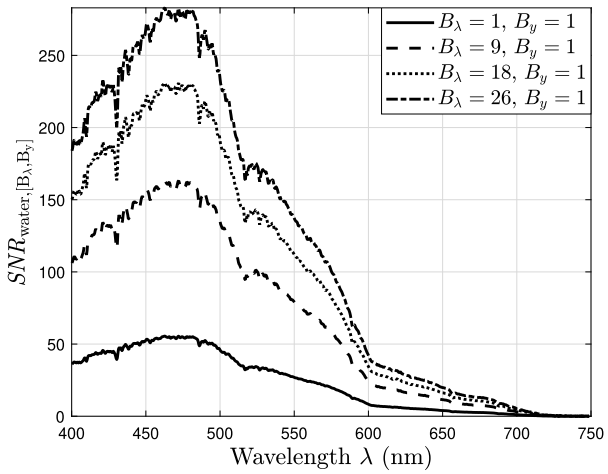

Fig. 6. SNR per pixel for the estimated $L_{\text{water}}^{\text{ToA}}$ with exposure time $\tau = 51.6$ ms and $B_\lambda = 1$, 9, 18, and 26 binning operations.

Simulated by using (7), (8) and (9), Fig. 6 shows the estimated $\text{SNR}_{\text{water}}$ at ToA for the wavelengths 400–750 nm where the hyperspectral imager observes the water-leaving radiance $L_{\text{ref}}^{\text{ToA}} = L_{\text{water}}^{\text{ToA}}$ in Fig. 5 for viewing angle $\gamma = 0^\circ$ and exposure time $\tau = 51.6$ ms. At a chosen wavelength of 500 nm, the SNR increases from $\text{SNR}_{\text{water},[1,1]} = 45.8$ to $\text{SNR}_{\text{water},[9,1]} = 134.8$ for $B_\lambda = 9$, $\text{SNR}_{\text{water},[18,1]} = 190.6$ for $B_\lambda = 18$, and $\text{SNR}_{\text{water},[26,1]} = 233.5$ for $B_\lambda = 26$. Given the stated assumptions, the estimated performance at $B_\lambda = 9$ conforms with the recommended SNR of at least 40–100 for atmospherically corrected water-leaving signals [42]. Moreover, the spectral bandpass is $\Delta\lambda = 3.33$ nm for no binning and up to $B_\lambda = 9$, whereas $B_\lambda = 18$ and $B_\lambda = 26$ give $\Delta\lambda = 6.67$ nm and $\Delta\lambda = 10$ nm, respectively.

IV. Remote Sensing Approach

A. Attitude Definition

Shown in Fig. 7, the orthogonal body frame unit vectors $\hat{\mathbf{x}}_b$, $\hat{\mathbf{y}}_b$ and $\hat{\mathbf{z}}_b$ are located at the satellite's center of mass and point along its principal axes of inertia. The hyperspectral imager is assumed mounted with its optical axis coinciding with $\hat{\mathbf{z}}_b$ and its slit width w_{slit} and height h_{slit} being placed along $\hat{\mathbf{x}}_b$ and $\hat{\mathbf{y}}_b$, respectively. The orbit frame is also located at the satellite's center of mass where $\hat{\mathbf{x}}_o$ coincides with the velocity vector, $\hat{\mathbf{y}}_o$ points toward the negative orbit normal, and $\hat{\mathbf{z}}_o$ corresponds to the nadir vector aligned with the negative position vector as seen in the Earth-centered-inertial (ECI) frame. For simplicity, it is assumed that the Earth is spherical such that the nadir vector $\hat{\mathbf{z}}_o$ coincides with the line defining the local altitude H. The orientation of the body with respect to the orbit frame are represented by the Euler angles ϕ, θ and ψ (roll, pitch and yaw), where $\phi = \theta = \psi = 0^\circ$ if the body frame coincides with the orbit frame. The attitude errors from reference angles ϕ_{ref}, θ_{ref}, ψ_{ref} are $\delta\phi = \phi_{\text{ref}} - \phi$, $\delta\theta = \theta_{\text{ref}} - \theta$, $\delta\psi = \psi_{\text{ref}} - \psi$. Furthermore, ω_x, ω_y, and ω_z are the angular velocities of the body frame relative to the orbit frame.

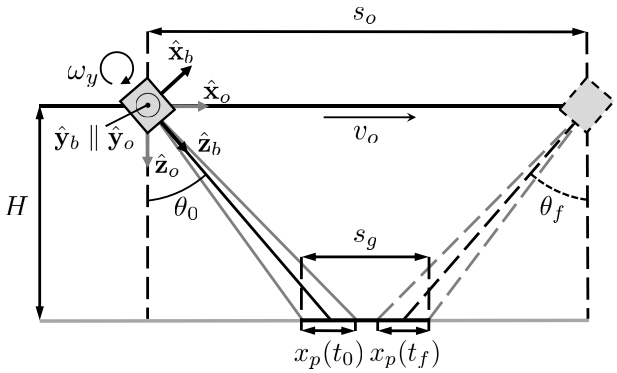

Fig. 7. Geometry of an imaging satellite at altitude H covering the distance s_o at orbital speed v_o. Images are collected along the ground length s_g while rotating with angular velocity ω_y from starting angle θ_0 to final angle θ_f. The instantaneous starting and final along-track footprint components are $x_p(t_0)$ and $x_p(t_f)$. The unit vectors $\hat{\mathbf{y}}_b$ and $\hat{\mathbf{y}}_o$ point out of this article here.

B. Instantaneous Resolution

The instantaneous footprint of the hyperspectral imager can be split into components along and perpendicular to its scan direction, calculated by using (1a) and (1b) such that

$$P_w = H \sec\phi \left(\tan\left(\theta + \frac{\epsilon_w}{2}\right) - \tan\left(\theta - \frac{\epsilon_w}{2}\right)\right) \quad (10a)$$

$$P_h = H \sec\theta \left(\tan\left(\phi + \frac{\epsilon_h}{2}\right) - \tan\left(\phi - \frac{\epsilon_h}{2}\right)\right) \quad (10b)$$

being transformed to along-track and cross-track components of a central pixel with respect to the velocity direction as

$$x_p \triangleq \cos(\psi) P_w + \sin(\psi)\frac{P_h}{N_y} \quad (11a)$$

$$y_p \triangleq \cos(\psi)\frac{P_h}{N_y} - \sin(\psi) P_w. \quad (11b)$$

In practice, the footprints of pixels toward the edge of the imager's swath are elongated compared to those of the central pixels. Along with effects from the Earth curvature, these distortions are known as the "bowtie effect" which can be corrected in post-processing [63], [64]. We note that the footprint is taken to be relatively small, i.e., on a meter scale per pixel, hence the "bowtie effect" can be ignored if a high frame rate and narrow FoV are considered.

C. Spatial Resolution

Adding translational and rotational effects during exposure time τ to the instantaneous footprint in (11a) and (11b), the along-track and cross-track components of the spatial resolution in a pixel are

$$\Delta x = x_p + v_{p,x}\tau \quad (12a)$$

$$\Delta y = y_p + v_{p,y}\tau \quad (12b)$$

where $v_{p,x}$ and $v_{p,y}$ are the along-track and cross-track velocity components of a pixel

$$v_{p,x} \triangleq v_o + \dot{\theta} H - \dot{\psi} H \tan(\phi) \quad (13a)$$

$$v_{p,y} \triangleq -\dot{\phi} H + \dot{\psi} H \tan(\theta) \quad (13b)$$

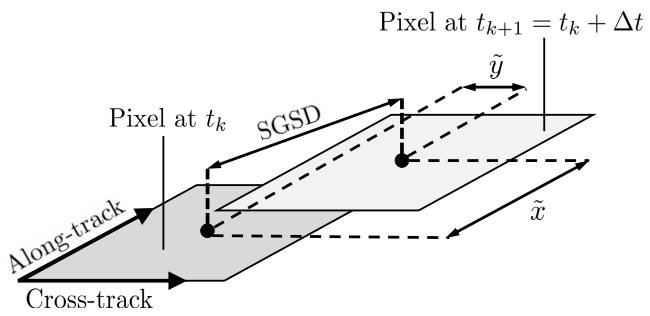

Fig. 8. SGSD is the distance on ground that the same pixel has shifted between first capture at time t_k and second capture at $t_{k+1} = t_k + \Delta t$, where Δt is the camera integration time.

with v_o being the satellite's orbital speed. Shown in Fig. 8, the SGSD is defined as the ground distance between the same pixel in two sequentially captured frames during integration time Δt, thus indicating how much the two frames overlap. The SGSD is expressed in along-track and cross-track components as

$$\tilde{x} \triangleq v_{p,x} \Delta t \tag{14a}$$

$$\tilde{y} \triangleq v_{p,y} \Delta t. \tag{14b}$$

Since x_p can be significantly larger than y_p when the pushbroom scan is aligned with the velocity direction, then it is preferred to slowly rotate about $\hat{\mathbf{y}}_o$ to enable better along-track SGSD. Noting from (13a) and (14a), the required pitch rate of the satellite $\dot{\theta}$ may be obtained from a desired $\tilde{x}$ or vice versa.

D. Image Acquisition Strategy

Consider the ground length s_g to be uniformly scanned during time $\Delta T = t_f - t_0$ where the satellite translates at a constant orbital speed v_o and rotates from starting pitch angle $\theta(t_0) = \theta_0$ to final pitch angle $\theta(t_f) = \theta_f$, as shown in Fig. 7. Assuming a local linear track for relatively short ΔT and small s_g, the final pitch angle can be set to $\theta_f = -\theta_0$ such that $x_p(t_0) = x_p(t_f)$. Furthermore, it is assumed that $\omega_x = \omega_z = 0$ rad/s and $\phi = \psi = 0°$ such that $\omega_y = \dot{\theta}$ [65].

Given these assumptions, the orbit track distance covered during the slew maneuver can be calculated as

$$s_o = s_g + 2H \tan\left(\theta_0 - \frac{\epsilon_w}{2}\right) \tag{15}$$

where the total time elapsed is

$$\Delta T = \frac{s_o}{v_o} \tag{16}$$

which then results in the constant reference angular velocity being obtained from

$$\omega_{\text{ref},y} = \dot{\theta}_{\text{ref}} = \frac{\Delta\theta}{\Delta T} = -\frac{2\theta_0}{\Delta T}. \tag{17}$$

Fig. 9 shows the plots of required angular velocity $\omega_{\text{ref},y}$ at $H = 500$ km as a function of $\theta_0 = -\theta_f$ for $s_g = 10$ km, 40 km, 80 km, and 500 km. Higher H or longer s_g demands slower rotation to achieve a constant SGSD.

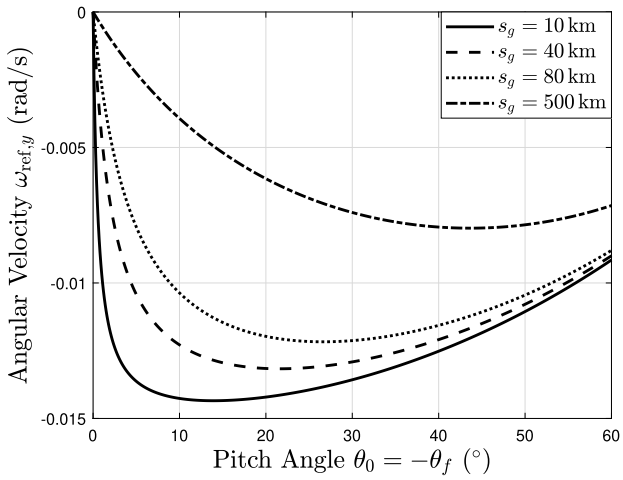

Fig. 9. Angular velocity $\omega_{\text{ref},y}$ versus pitch angles $\theta_0 = -\theta_f$ required for uniformly imaging $s_g = 10$ km, 40 km, 80 km, and 500 km at $H = 500$ km.

TABLE II
SIMULATION PARAMETERS FOR IMAGE ACQUISITION

Parameter	Value
Frame rate FPS	18
Camera integration time Δt	55.6 ms
Camera exposure time τ	51.6 ms
Camera read-out time δt	4 ms
Altitude H	500 km
Orbital speed v_o	7.61 km/s
Target ground length s_g	40.08 km
Roll angle ϕ	0°
Yaw angle ψ	0°

E. Simulation Results

1) Resolution at Nadir: Using the parameters in Tables I and II, and assuming the scan is nadir-pointing and aligned with the satellite's velocity direction, the along-track and cross-track components of a pixel footprint become $x_p = 500$ m and $y_p = 58.6$ m with a swath width of $P_h = 40.08$ km. The along-track and cross-track spatial resolution are $\Delta x = 892.5$ m and $\Delta y = 58.6$ m, respectively, and the along-track SGSD is $\tilde{x} = 422.9$ m meaning that 3 frames partially overlap by 422.9 m. Moreover, it takes $\Delta T = 5.2$ s to scan the ground length $s_g = 40.08$ km while nadir-pointing.

2) Resolution During Slew Maneuver: Assuming $\omega_y = \omega_{\text{ref},y}$ without any attitude errors, and using the parameters in Tables I and II, Figs. 10 and 11 show how the spatial resolution varies with slew maneuvers starting at θ_0 at 0°, 10°, 20° and 30°, and ending at the corresponding $\theta_f = -\theta_0$. For these four configurations, Table III indicates the required angular velocities, observation time and the obtained along-track SGSD. For example, choosing $\theta_0 = 20°$ and $s_g = 40.08$ km, the satellite would have to rotate with $\omega_y = -0.0132$ rad/s for $\Delta T = 53.1$ s to achieve a constant along-track SGSD of $\tilde{x} = 57.6$ m. In this case, the along-track spatial resolution varies from $\Delta x = 619.6$ m at $\theta = 20°$ to $\Delta x = 553.4$ m when crossing nadir, whereas the cross-track spatial resolution varies from $\Delta y = 62.4$ m at $\theta = 20°$ to

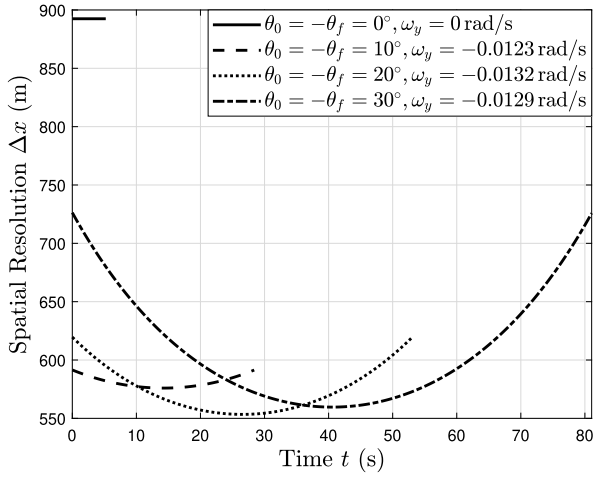

Fig. 10. Along-track spatial resolution Δx during a scan for chosen configurations of pitch angles $\theta_0 = -\theta_f$ and angular velocity ω_y.

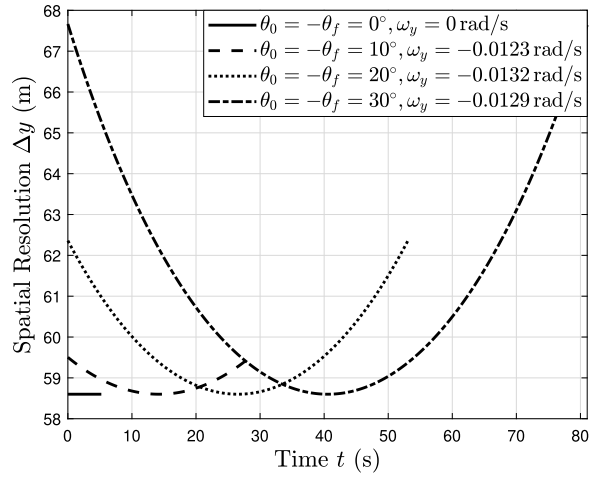

Fig. 11. Cross-track spatial resolution Δy during a scan for chosen configurations of pitch angles $\theta_0 = -\theta_f$ and angular velocity ω_y.

$\Delta y = 58.6$ m at nadir. For $\tilde{x} = 57.6$ m there will be at least 10 frames that partially overlap in the along-track direction. With this many overlapped spatial pixels of the same scene, the effective SNR in the image may theoretically increase up to $\sqrt{10}$ times, i.e., 83% more than for a nadir-pointing scan.

3) Attitude Error Requirements: Precise attitude control is essential to obtain the desired SGSD at any time during image acquisition. Referring to the recommended 100 m spatial resolution discussed in Section II, the requirement for accuracy in angular velocity can be calculated by using (13a) and (14a) such that

$$|\delta\dot{\theta}| \leq \frac{|x^* - \tilde{x}|}{H\,\Delta t} - \frac{v_o}{H} + \dot{\psi}\tan(\phi) - \dot{\theta}_{\text{ref}} \tag{18}$$

where x^* is the upper limit of SGSD set between two sequential frames. It can be assumed that $\dot{\psi}\tan(\phi) \approx 0$ if ϕ and $\dot{\psi}$ are small. Using the parameters in Table II, and choosing an reference angular velocity of $\dot{\theta}_{\text{ref}} = \omega_{\text{ref},y} = -0.0132$ rad/s, along-track SGSD of $\tilde{x} = 57.6$ m, and setting $x^* = 100$ m, the angular velocity errors must be less than 0.0016 rad/s throughout the whole image acquisition.

TABLE III
SLEW MANEUVER RESULTS FOR $s_g = 40.08$ km AND FPS $= 18$

θ_0 (°)	ω_y (rad/s)	ΔT (s)	$\tilde{x}$ (m)	$\lvert\delta\hat{\theta}\rvert$ (°)
0	0	5.2	422.9	0.0088
10	−0.0123	28.4	81.8	0.0111
20	−0.0132	53.1	57.6	0.0102
30	−0.0129	81.1	64.3	0.0086

The attitude error problem can be relaxed to rather focus on obtaining sufficient attitude knowledge for consistent image registration or georeferencing. Assuming no uncertainty in position and a precise onboard time synchronization, then for pixel-to-pixel distance errors to remain within the bound of $|x^*|$, the attitude knowledge error requirement can be calculated as

$$|\delta\hat{\theta}| \leq \tan^{-1}\left(\frac{|x^*|}{H\sec(\phi)} + \tan(\theta_{\max})\right) - \theta_{\max} \tag{19}$$

where $\theta_{\max}$ is the largest angle during image acquisition. Given $x^* = \pm 100$ m at $\theta_{\max} = 20°$ and $\phi = 0°$, and assuming $\sec(\phi) \approx 1$, the required attitude knowledge accuracy must be better than 0.01°. The required attitude knowledge accuracy for the other three slew maneuver configurations are indicated in the rightmost column in Table III.

V. HYPSO-1 SYSTEM

A. Satellite Bus

The hyperspectral imager is adapted to the Multipurpose 6U Platform (M6P), shown in Fig. 12, with a mass of approximately 6.8 kg when fully integrated. The M6P is a commercially available nanosatellite bus provided by NanoAvionics. It has 16 bodymounted triple-junction Gallium Arsenide solar cells and six Lithium-Ion batteries with a total energy capacity of 64.9 Wh. Among its important subsystems are a flight computer (FC) for onboard data handling and ADCS functions, a SatLab global navigation satellite system (GNSS) for orbit determination and time synchronization, an electrical power system (EPS) for power management, a ultrahigh frequency (UHF) radio for basic space–ground communications, and a payload controller (PC) working as a storage device and router between the payload and satellite bus. The internal bus communications utilize the CubeSat space protocol (CSP) over a controller area network (CAN) where each subsystem is a network node with its dedicated CSP address.

B. Dedicated Subsystems

To accomplish the CONOPS described in Section II, the HYPSO-1 satellite bus is further equipped with:

1) a Nano Star Tracker ST-1 [66] and Sensonor STIM210 Inertial Measurement Unit (IMU) [67] for precise attitude determination during imaging. The sensors are turned on for at least 5 min before use to ensure sufficient settling time after initialization. When imaging operations are not scheduled, then six sun sensors, three

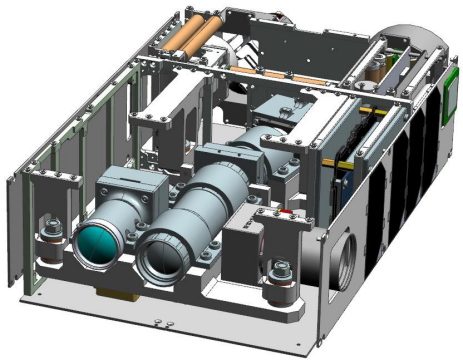

Fig. 12. Computer-aided drawing (CAD) model of HYPSO-1 with its top and front solar panels removed. The hyperspectral imager can be seen in the center with an RGB camera to its left and a star tracker to its right.

magnetometers, and three gyroscopes are used instead which provide coarser attitude knowledge but consume much less power;

2) four reaction wheels used for attitude control, three being placed orthogonally along the satellite's body axes and the fourth being tilted at 54.7°. Each reaction wheel provides up to 3.2 m · Nm torque. Magnetorquers are also placed along each body axis for reaction wheel momentum dumping;
3) an IDS UI-125x Red-Green-Blue (RGB) camera with a 6 mm $F/1.4$ Ci series fixed lens, providing a footprint of 770 km × 540 km and spatial resolution of approximately 500 m. Its main purpose is to support and validate the hyperspectral images in the spatial domain [68];
4) a 2.4-GHz IQ Spacecom S-band transceiver provided by IQ Wireless with a usable data rate of 1 Mb/s for downlinking payload data; and
5) an Onboard Processing Unit (OPU) hosting a Zynq-7030 Xilinx PicoZed System-on-a-Chip (SoC) with flight heritage [33], which consists of two ARM core processors and a Field-Programmable Gate Array (FPGA) for onboard image processing. The OPU allows for in-orbit software updates and FPGA hardware reconfigurations for algorithms or upgrades that can be uploaded from the ground. The payload data are stored on a secure digital (SD) card with 8 GB (Gigabytes) space, wherefrom larger amounts can be buffered to the PC over CAN before downlink through the S-band radio. Smaller amounts can be downloaded directly from the OPU if needed, although buffering the data to the PC generally enables full utilization of the S-band data rate and avoids keeping the OPU turned on for longer than necessary. Furthermore, the OPU hosts a custom breakout board with PicoZed interfaces that provide power and data lines to the hyperspectral and RGB cameras.

C. Power Budget

M6P's solar arrays generate about 11.65 W during 58.9 min in sunlight out of an orbital period of 94.6 min. To estimate if HYPSO-1's energy is sufficient during burdensome operations,

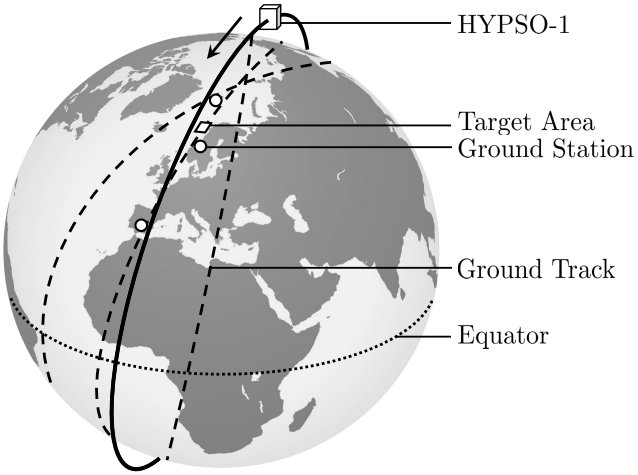

Fig. 13. Position of HYPSO-1 in SSO at 10:25:00 UTC 28 May 2022. Selected ground stations are marked by white circles and the target area by a white square (here in Lofoten, Norway). Previous, current and successive ground tracks are indicated by dashed lines.

TABLE IV
HYPSO-1 POWER BUDGET IN ONE ORBITAL REVOLUTION

Subsystem	Power (W)	DC (%)	Power Used (W)
Hyperspectral imager	3.675	1.09	0.040
RGB camera	3.375	0.55	0.020
OPU imaging	4.234	1.09	0.046
OPU image processing	4.234	6.69	0.283
OPU-PC transfer	4.234	35.33	1.496
ADCS cruise	3.441	94.72	3.259
ADCS precise	6.331	5.28	0.334
S-band radio RX	4.813	10.57	0.509
S-band radio TX+RX	12.201	10.57	1.290
Other	1.530	100	1.530
Total (+10% margin)			9.688
Generated			9.861
Remaining			+0.174

the power budget assumes uplink, imaging, onboard processing, and downlink are all happening during one orbital revolution. This scenario is illustrated in Fig. 13, where instructions are first uplinked from KSAT in Svalbard before HYPSO-1 observes a target area in Lofoten, Norway, and downlinks as much data as possible to NTNU Trondheim and KSAT in Spain in one pass while being exposed to the sun.

Table IV shows power budget with 5% component margins and the corresponding duty cycles (DCs). Battery input and output efficiencies are assumed 92% each. Power consumed in OPU, ADCS, and S-band radio are split into more than one operational mode, whereas "Other" denotes the collective power consumption by FC, EPS, PC, and internal communications. "ADCS precise" indicates preparing for and executing a slew maneuver during imaging when both the IMU and star tracker are active, consuming up to 1.5 W each.

Naturally, peaks in HYPSO-1's power consumption are expected during image acquisition, onboard image processing, and downlink. Adding a 10% system margin results in remaining power of about 174 mW. Enforcing the power budget to stay positive and safe, the maximum allowed duration is set to 6.33 min for onboard image processing and 33.42 min for buffering data from OPU to PC. Allowed duration for data

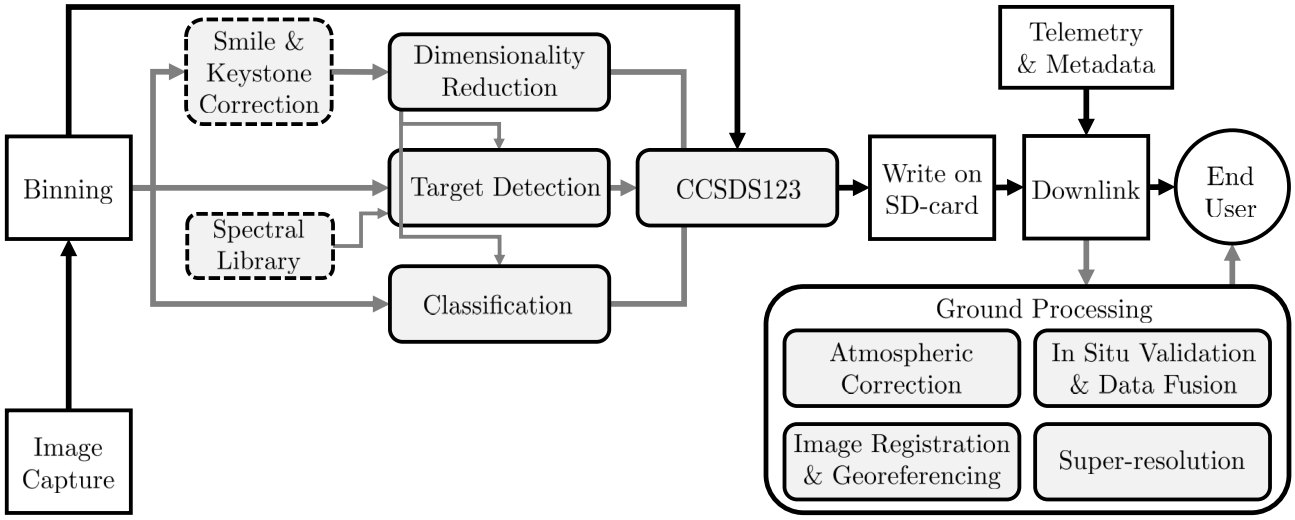

Fig. 14. Block diagram of the proposed onboard image processing pipelines. In order, the hyperspectral images are captured, binned, processed at a chosen level, stored on the SD card, and downlinked together with telemetry and metadata. Depending on the chosen data product, additional ground-based processing and fine-tuning can be applied before distribution to end-users. Black arrows indicate the minimal onboard processing pipeline whereas gray arrows are the alternative routes for tailored data products.

TABLE V
HYPERSPECTRAL DATA PRODUCTS FOR $N_x \times N_y = 956 \times 684$ SPATIAL PIXELS

Level	Bands/Components	Pixel size (b)	Total size (MB)	Reduction (%)	Speed (Mb/s)
Raw with binning of $B_\lambda = 9$	120	16	156.94		
CCSDS123 (MOBIP)	120	16	69.75	55.6	6 260[a]
PCA (DROBIP)	20	16	11.89	92.4	268.6[b]
OTFP (DROBIP)	20	16	11.89	92.4	7[c]
EMSC (DROBIP)	20	16	11.89	92.4	54.5[d]
Target detection (TOBIP)	1	16	1.308	99.2	903.1[d]
Classification — 16 classes (COBIP)	1	4	0.331	99.8	53.2[c]
Classification — 256 classes (COBIP)	1	8	0.711	99.6	53.2[c]

[a] measured on Zynq-7030 Xilinx FPGA flight hardware on the OPU.
[b] estimated from Xilinx Virtex-7 XC7VX690T FPGA-based software/hardware co-design tests on hyperspectral data of similar size.
[c] estimated from software implementation tests on hyperspectral data of similar size.
[d] estimated from Zynq-7000 FPGA-based software/hardware co-design tests on hyperspectral data of similar size.

transmission through S-band radio is set to 10 min which allows downlinking up to 75 MB (Megabytes) of data per orbital revolution.

VI. ONBOARD IMAGE PROCESSING ARCHITECTURE

A. Overview

The OPU's FPGA-based image processing algorithms are key in enabling faster data download and distribution while at the same time relieving HYPSO-1's power budget. The idea behind its image processing architecture is to support modular arrangements of algorithms, or pipelines, as illustrated in Fig. 14. The minimal onboard image processing pipeline (MOBIP), dimensionality reduction onboard image processing pipeline (DROBIP), target detection onboard image processing pipeline (TOBIP), and classification onboard image processing pipeline (COBIP), are designed to generate hyperspectral data products that are tailored to the immediate needs of an user or operator. Useful satellite and payload telemetry and other relevant metadata, e.g. attitude and position, are also downlinked together with the processed data.

Table V shows the expected size reduction and processing speeds for the algorithms to be employed in the architecture. A raw hyperspectral datacube with 956×684 spatial pixels and 1080 spectral pixels binned $B_\lambda = 9$ times is considered as the starting point before any processing. "Bands/Components" represent spectral bands for both the raw data and MOBIP, extracted components for DROBIP, a probability map of detected spectral target signatures for TOBIP, and a layer containing spectral-based classes for COBIP. The data size reduction and processing speed estimates are based on reported performances of state-of-the-art algorithms having been applied on various hyperspectral data of similar sizes. For the relevant algorithms implemented in FPGA, more details related to their occupation, execution time, operating frequency, and latency can be found in the respective literature where indicated in Sections VI-B–VI-D.

B. Minimal Onboard Image Processing

MOBIP consists of only the CCSDS123v1 lossless compression algorithm [69], being employed after image acquisition, time-stamping, and binning. A Direct Memory Access (DMA) solution, CubeDMA, is built into the FPGA to ensure efficient streaming of the hyperspectral images by excluding the Central Processing Unit (CPU) from its critical path of

transfer and establishing direct communication link between memory and the dedicated CCSDS123v1 processing core [70]. The CCSDS123v1 proposed in [71] and [72] offers a FPGA core speed of up to 9984 Mb/s obtained on Zynq-7030 Xilinx PicoZed, however, slightly lower speed is measured when running in the whole pipeline on HYPSO-1's OPU. With the raw binned image as a starting point, a 55.6% compression is achieved as shown in Table V, i.e., a size reduction of 2.25 times. Without any loss of spatial-spectral information, this general data product can be independently processed and analyzed further by any user on the ground.

C. Onboard Image Processing for Tailored Data

Given the FPGA reconfigurability in HYPSO-1, several suitable algorithms for DROBIP, TOBIP, and COBIP are described here. Some have already been demonstrated as FPGA-implementations or software/hardware codesigns in relevant hardware, although a few still run in pure software and need more development for onboard implementation.

1) Dimensionality Reduction: Dimensionality reduction methods extract the main spectral patterns and remove redundancies from the high-dimensional hyperspectral data. Spatial-spectral features of interest can therefore be utilized for specifically studying the relevant water-leaving signals and atmospheric effects. Because the data redundancies are removed, then improved overall computational efficiency may also be obtained if applied as a preprocessing step in a pipeline [73]. Shown in Table V with 20 components chosen for DROBIP, a 92.4% reduction in size is estimated if dimensionality reduction is combined with CCSDS123v1. As an optional step before dimensionality reduction, smile, and keystone corrections can prevent intertwining systematic artifacts by adjusting the images to account for optical and measurement noise inherent to the imager [74].

A common dimensionality reduction technique is the principal component analysis (PCA) which obtains a reduced and denoised subspace representation of the raw hyperspectral data, assuming a linear model with Gaussian noise [75]. The extracted spatial-spectral information of a scene is contained in only a few principal components instead of several dozens or hundreds of spectral bands. An FPGA implementation of PCA in Xilinx Virtex-7 XC7VX690T proposed in [76] obtains a computation time of 4.17 s for extracting 24 principal components from an Airborne visible/infrared imaging spectrometer (AVIRIS) image of Jasper Ridge Biological Preserve, California, with 614×512 spatial pixels and 224 spectral channels, which can be fast enough to process a stream of hyperspectral images in real-time. Proposed in [77], an adaptive PCA-based On-the-Fly Processing (OTFP) algorithm may sequentially process streaming blocks of high-dimensional data instead of analyzing the whole dataset at the end of image acquisition. Implemented in MATLAB, OTFP's reported computation time is 300.2 s for obtaining 3 principal components from a 16-bit hyperspectral image of 1000×245 spatial pixels and 450 spectral channels, although higher speed is expected for an FPGA implementation. An alternative to PCA, the extended multiplicative signal correction (EMSC) estimates a denoised subset of relevant spectra using a linear statistical model of observations with approximated light absorbance and scattering [78]. Our software/hardware codesign of a prototype EMSC on a Zedboard development platform with ARM Cortex-A9 processor measured a computation time of 3.81 s when applied on a 16-bit hyperspectral datacube with 500×500 spatial pixels and 50 spectral channels.

2) Target Detection: Hyperspectral images of heterogeneous scenes are amenable to spectral-based target detection because of their numerous spectral bands [79], [80]. An efficient use of such algorithms requires a set of *a priori* known target spectra and high spatial resolution to reduce the effects of spectral mixing. Target detection essentially creates a probability map of specific spectral signatures across the spatial domain of the image, resulting in a 2-D data product per chosen number of signatures. As an example for TOBIP, only one target signature is chosen in Table V such that the size of the 2-D map is $1 \times 956 \times 684 \times 16$ b $= 1.308$ MB, i.e., a size reduction of approximately 99.2% when compared to the original data. Additional lossless compression is therefore not needed due to the already small data product size.

The target detection module proposed in [81] supports constrained energy minimization (CEM), adjusted spectral matched filter (ASMF), and modified adaptive cosine estimator (ACE) detectors to determine the likelihood of specific spectral signatures in a spatial pixel. A software/hardware codesign of modified ACE algorithm on a Zedboard development platform with ARM Cortex-A9 processor reports a computation time of 3.29 s for the input of a 16-bit HyMap hyperspectral datacube with 224 000 spatial pixels and 16 principal components using PCA preprocessing [82]. Taken to be the speed estimate in Table V, a computation time of 0.5 s is reported for an FPGA-implementation of the modified ACE algorithm on Zynq-7035 SoC (Kintex-7) when applied on the same HyMap datacube with 126 spectral bands and no preprocessing [81].

3) Classification: Using a spatial-spectral classification framework, the spatial pixels in a hyperspectral image can be distinguished into various classes formed by specific spectral signatures [83]. One of many such classification techniques being suitable for FPGA-implementation is the fast spectral clustering (FSC), which is a graph-based unsupervised method and does not require training data [84], [85]. Indicated in Table V, it is possible to represent each layer with a 4-bit integer for fewer than 16 classes whereas 256 classes requires 8 bits. The size of 16 class signatures with 120 spectral bands per signature is therefore $16 \times 120 \times 16$ b $= 0.0038$ MB and $256 \times 120 \times 16$ b $= 0.0614$ MB for 256 class signatures. These auxiliary data products supplement the classification map with size of $1 \times 956 \times 684 \times 4$ b $= 0.327$ MB for 16 classes and $1 \times 956 \times 684 \times 8$ b $= 0.654$ MB for 256 classes, giving a total data size reduction of 99.8% and 99.6%, respectively. Due to the already small data sizes obtained from classification alone, the reduction factors for COBIP in Table V do not include any lossless compression.

The Nystrøm extension clustering version of FSC, described in [84], is estimated to have a processing speed of about

245.8 Mb/s based on its MATLAB implementation. It reports 1.62 s computation time for obtaining 16 classes from a 16-bit AVIRIS image of Salinas Valley, California, with 512×217 spatial pixels and 224 spectral bands, although higher speed is expected for a software/hardware codesign of FSC in FPGA. An alternative to FSC is the clustering using binary partition trees (CLUS-BPT) framework which integrates embedded hyperspectral data segmentation, region modeling, feature extraction by PCA, and clustering [86]. Also in MATLAB, it has a reported computation time of 7.48 s for the same AVIRIS image, indicating that FSC generally outperforms the CLUS-BPT in terms of speed if an input image has very large dimensions. The estimated processing speed is therefore assumed to be 53.2 Mb/s based on the CLUS-BPT as a worst case in Table V. As with any other algorithms, cropping the images in the spatial domain to rather focus on specific regions can further relieve the computation time.

D. Discussion on Advanced Algorithms

Beyond those already described, other relevant algorithms may potentially be uploaded to HYPSO-1 given that their operational maturity is reached for use in FPGA. For the interest of the HYPSO-1 mission, candidate algorithms may include image registration, georeferencing, atmospheric correction, and super-resolution which may contribute to improved accuracy in dimensionality reduction, target detection, and classification. However, such algorithms are currently too computationally intensive and complex for onboard implementation. Before any upload of these, they should first undergo prototyping and rigorous testing on the ground with careful validation with respect to speed, reliability, and accuracy.

1) Image Registration: The relative separation between individual pixels is determined by image registration, also known as orthorectification. Image registration algorithms are too computationally expensive for onboard implementation in general [87], but a potential candidate is the ray-tracing method which is simpler and has been prototyped for joint registration and georeferencing, similar to the one described in [88].

2) Georeferencing: The benefit in onboard georeferencing for HYPSO-1 lies in directly downlinking latitude and longitude coordinates of the image pixels together with extracted results from target detection or classification, requiring precisely time-synchronized attitude and position data. Using georeferencing on the ground instead, it is possible to download only the relevant pixel indices where positive target detection or classification have been made, and then identifying them with the correct geodetic coordinates. The latter can therefore be used to quickly direct any nearby *in situ* asset to the locations of interest in HYPSO-1's observed area.

3) Super-Resolution: The spatial resolution in images can be enhanced using super-resolution algorithms as described in [89], which may also result in improved radiometric and geometric accuracy in the data. Prototypes for super-resolution, e.g., those based on multiframe super-resolution [90], [91], require a measurement process in determining the point spread function (PSF) to infer higher spatial resolution [92], [93]. However, when estimating the PSF, these methods can be susceptible to noise, quantization, compression, and inaccuracies [94], [95]. Prior-based super-resolution techniques, e.g., sparse image representations [96] and convolutional neural nets [97], [98], overcome these limitations in the measurement-based techniques by supplying input pixels with the expectations of hyperspectral image statistics. Other alternatives involve using multispectral-hyperspectral image fusion [99], [100], and super-resolution based on dimensionality reduction [101].

Proposed in [102] and being under development, a Richardson–Lucy (RL) deconvolution algorithm implemented on a Xilinx Zynq-7020 Zedboard with two ARM Cortex-A9 cores has been successfully applied on hyperspectral data. A computation time of 1.06 ms per iteration is reported for processing 150×640 pixels with one spectral band using a kernel size of 9×9 pixels. A corresponding software/hardware codesign of the RL algorithm is described in [103].

4) Atmospheric Correction: Removing atmospheric effects in the hyperspectral data before dimensionality reduction, target detection or classification, can improve efficiency and accuracy in extracting the relevant water-leaving signals. The purpose of atmospheric correction is to identify all terms in (6) that contribute to the total ToA radiance $L_{\text{total}}^{\text{ToA}}$, and predict the actual water-leaving radiance L_{water} which may further contain the relevant optical properties of water constituents, e.g., chlorophyll.

Several ground-based atmospheric correction schemes work well for open ocean water scenes in multispectral data [54], [104]–[106], and good performance has also been shown for hyperspectral imagery of coastal waters [107]. The traditional atmospheric correction methods are generally based on the radiative transfer model [37], and are, in principle, not designed for onboard use due to their complexity and computational expense. Without contemporary empirical or ground truth data, they can also be prone to over- or undercorrection of the terms in (6), resulting in significant radiometric inaccuracies for a highly variable atmosphere and heterogeneous coastal waters. However, nondeterministic atmospheric correction methods that use machine learning, e.g., neural networks, have been regularly employed and are considered to be effective when given a proper set of training data [106]. If hyperspectral images or ground truth data are unavailable for training, then tools such as accurate radiative transfer (AccuRT) [108] could simulate the heterogeneous and coupled water-atmosphere scenes to be utilized instead [109]. Regardless, such atmospheric correction methods need further development and testing before any suitable onboard implementation in HYPSO-1.

E. Dynamic Reconconfiguration

Using dynamic reconfiguration (DR) on the OPU's FPGA enables both changes and adaptation in onboard processing. The DR can also better utilize resources by switching between different processing pipelines and incorporates functional updates and upgrades being uplinked from the ground.

TABLE VI
PERFORMANCE FOR SELECTED HYPERSPECTRAL IMAGER MODES

Type	Mode A	Mode B	Mode C	Mode D	Mode E
ADCS Mode	Slew	Slew	Slew	Nadir	Nadir
AoI (pixels)	$1\,080 \times 684$	$1\,080 \times 684$	$1\,080 \times 1\,194$	$1\,080 \times 1194$	$1\,936 \times 1\,216$
Binning B_λ (pixels)	9	18	9	9	1
Spectral range (nm)	387–801	387–801	387–801	387–801	220–967
Spectral bands	120	60	120	120	215
Bandpass $\Delta\lambda$ (nm)	3.33	6.67	3.33	3.33	3.33
Frame rate FPS	18	12	12	12	104
Exposure time τ (ms)	51	79	79	79	96
Scan duration ΔT (s)	53.08	53.08	57.00	9.19	1.00
Number of frames N_x	956	637	685	111	10
Scan distance, along-track s_g (km)	40.08	40.08	69.97	69.97	7.60
Swath width P_h (km)[a]	40.08	40.08	69.97	69.97	69.97
Spatial resolution, along-track Δx (m)[a,b]	553	582	618	1101	1231
Spatial resolution, cross-track Δy (m)[a,b]	58.60	58.60	58.60	58.60	58.604
SGSD, along-track $\tilde{x}$ (m)	57.6	86.3	124.1	634.4	761.3
$SNR_{\text{water},[B_\lambda,1]}$ @470 nm[a]	158.1	196.3	197.4	197.4	217.9
Data size, raw (MB)	156.94	52.28	196.29	31.81	4.71
MOBIP data size (MB)	69.75	23.24	87.24	14.14	2.09
Onboard processing time (s)[c]	5.8	1.9	7.2	1.2	0.2
OPU-PC transfer time (s)[c]	1 924.1	641	390	2 406.7	57.7
Downlink time (s)[d]	558.0	185.9	697.9	113.1	16.7
DROBIP data size (MB)[e]	11.62	7.75	14.54	2.36	0.22
Onboard processing time (s)[e]	5.6	2.2	7.0	1.1	0.2
OPU-PC transfer time (s)[c]	320.7	213.7	401.1	65.04	6.0
Downlink time (s)[d]	93.0	62.0	116.3	18.8	1.7
TOBIP data size (MB)[e]	1.31	0.87	1.64	0.27	0.02
Onboard processing time (s)[e]	8.9	3.0	11.1	1.8	0.29
OPU-PC transfer time (s)[c]	36.1	24.0	45.1	7.3	0.7
Downlink time (s)[d]	10.5	7.0	13.1	2.1	0.2
COBIP data size (MB)[e]	0.33	0.22	0.41	0.07	0.01
Onboard processing time (s)[e]	23.6	7.9	29.6	4.8	0.8
OPU-PC transfer time (s)[c]	9.1	6.1	11.4	1.9	0.4
Downlink time (s)[d]	2.6	1.8	3.3	0.6	0.1

[a] viewing at nadir.
[b] spatial resolution in one frame, not the final image resolution by utilizing SGSD in e.g. image registration and super-resolution.
[c] includes time used for running on memory in the OS and writing data to SD-card at $100\,\mathrm{Mb/s}$.
[d] total time required for $1\,\mathrm{Mb/s}$ downlink data rate with S-band radio.
[e] estimated based on Table V.

An advanced ability in modern FPGAs is the dynamic partial reconfiguration (DPR) that reprograms only portions of the FPGA, while the rest of the system continues to operate. The DPR allows time-multiplexing of mutually time-exclusive algorithms/steps on a finer scale of the available resources and is characterized by shorter reconfiguration times as the FPGA configuration time is directly proportional to its bitstream size. DPR can also be used for applications such as mitigation and recovery from single-event upsets (SEUs) and for dynamic and adaptive real-time image processing.

Furthermore, the OPU also has a "golden image" that enables booting a previous version of a steady onboard processing configuration. In the case of corruption or any unwanted updates and upgrades received from the ground, the OPU will automatically revert to the "golden image."

F. Ground Support

Several algorithms run on the ground to adjust, fine-tune, and prepare data for end-users; assist in the in-orbit calibration of the hyperspectral imager; and rigorously test accuracy and reliability in updates or upgrades before uploading them to HYPSO-1. As indicated at the bottom right in Fig. 14, advanced modules such as image registration, georeferencing, atmospheric correction, and super-resolution are initially dedicated for use on the ground because they require prompt access to reference libraries and are highly complex and computationally expensive in their current state. In-orbit upgrades and extensions to the onboard image processing pipelines may include versions of these algorithms only if maturity for FPGA implementation is first demonstrated on the ground.

G. Data Latency in Typical HYPSO-1 Operations

Table VI shows HYPSO-1's remote sensing performance for five selected hyperspectral imaging modes and their corresponding data size and latency for data products generated by MOBIP, a PCA-based DROBIP, TOBIP containing only one 2-D map, and COBIP containing 16 classes. For each pipeline, the chosen number of spectral channels, the pixel size in bits, reduction factors, and processing speeds are assumed to be the same as in Table V. The SNR is calculated using the MOBY water-leaving radiance sensed at ToA as described in Section III-C. The ADCS modes with slew maneuvers are set with an angular velocity $\omega_y = -0.0132$ rad/s from starting angle $\theta_0 = 20°$ to final angle $\theta_f = -20°$ with $\phi = \psi = 0°$, and are assumed to have no attitude errors. The swath width, spatial resolution and SGSD are calculated in the manner described in Sections IV-B and IV-C.

From Table VI, it can be seen that the hyperspectral imaging modes A and B provide higher spatial resolution but narrower swath for an observed area size of approximately 40 km

TABLE VII
MODE A DATA LATENCY FOR HYPSO-1 ON EXAMPLE DATE 28 MAY 2022

	MOBIP	(69.75 MB)	DROBIP	(11.62 MB)	TOBIP	(1.31 MB)	COBIP	(0.33 MB)
Sequence	Start time	Duration (s)	Start time	Duration (s)	Start time	Duration (s)	Start time	Duration (s)
Orbit 1								
Image acquisition	10:29:40.0	53.1	10:29:40.0	53.1	10:29:40.0	53.1	10:29:40.0	53.1
Onboard processing	10:30:33.1	5.8	10:30:33.1	5.6	10:30:33.1	1.5	10:30:33.1	23.6
OPU to PC transfer	10:30:38.9	1 924.1	10:30:38.7	320.7	10:30:34.6	36.1	10:30:56.7	9.1
Downlink NTNU	—	—	—	—	10:31:10.7	10.5	10:31:05.8	2.6
Downlink KSAT Spain	—	—	10:35:59.4	93.0	—	—	—	—
Cruise	11:02:43.0	434.7	—	—	—	—	—	—
Eclipse	11:09:56.7	2 145.0	—	—	—	—	—	—
Orbit 2								
Cruise	11:45:42.0	630.0	—	—	—	—	—	—
Downlink KSAT Svalbard	11:56:12.0	276.0	—	—	—	—	—	—
Downlink NTNU	12:00:48.0	282.0	—	—	—	—	—	—
Total latency (min)		95.85		7.87		1.69		1.47

TABLE VIII
MODE A DATA LATENCY FOR HYPSO-1 WITHOUT CAN OVERHEAD ON EXAMPLE DATE 28 MAY 2022

	MOBIP	(69.75 MB)	DROBIP	(11.62 MB)	TOBIP	(1.31 MB)	COBIP	(0.33 MB)
Sequence	Start time	Duration (s)	Start time	Duration (s)	Start time	Duration (s)	Start time	Duration (s)
Image acquisition	10:29:40.0	53.1	10:29:40.0	53.1	10:29:40.0	53.1	10:29:40.0	53.1
Onboard processing	10:30:33.1	5.8	10:30:33.1	5.6	10:30:33.1	1.5	10:30:33.1	23.6
Downlink NTNU	10:30:38.9	316.0	10:30:38.7	93.0	10:30:34.6	10.5	10:30:56.7	2.6
Downlink KSAT Spain	10:35:54.9	242.0	—	—	—	—	—	—
Total latency (min)		8.62		2.53		1.09		1.32

by 40 km, whereas modes C and D provide coarser spatial resolution and wider swath for an 70 km by 70 km area size. Modes A, B, C and D use 1080 out of 1936 spectral pixels to approximately match the relevant wavelengths 400–800 nm. Lastly, mode E uses the full sensor resolution and is dedicated to diagnostics and in-orbit calibration during HYPSO-1's commissioning phase. "Onboard processing time" is the computation time for a particular pipeline, "OPU-PC transfer time" is the time to complete data buffering from OPU to PC at a speed of 290 kb/s, and "Downlink time" is the total time required to downlink all data through S-band radio at a bandwidth of 1 Mb/s. It is also assumed that the onboard data are written to the SD-card at a speed of 100 Mb/s which is included in "Onboard processing time."

From Table VI, we extend the results for the context of a typical mission scenario where HYPSO-1 uses mode A to observe a 40 km $\times$ 40 km area near Lofoten, Norway, then immediately aims to downlink a particular data product to the ground stations at NTNU Trondheim and KSAT in Svalbard and Spain with elevation angles assumed to be 5°, 2°, and 8°, respectively. Simulated using an orbit propagator in Analytical Graphics, Inc., (AGI) Systems Toolkit (STK) with epoch date set to 28 May 2022, the resulting time in UTC and durations of each sequence are shown in Table VII with OPU-PC overhead and in Table VIII without the overhead. A dash ("—") indicates that the operation is not available or necessary. "Cruise" means that HYPSO-1 is harvesting solar energy and "Eclipse" means that it is in Earth's shadow. Taking into account the overhead in OPU-PC transfer, all data products except for the one from MOBIP can be downloaded in less than 10 min. If there is no such overhead, then the MOBIP data product can also be made available in less than 10 min.

The reason for the bottleneck in OPU-PC transfer is that the current hardware and software architecture in HYPSO-1 is limited by the CAN communications interface between OPU and PC with a data rate of only 290 kb/s. This adversely impacts the overall latency for larger amounts of data as indicated in Table VII. In future planned missions, the physical interface may be replaced with a data bus capable of much higher throughput, i.e., using Ethernet or RS-422. Larger amounts of data can then be directly downloaded from the OPU, resulting in better latency as shown in Table VIII.

VII. CONCLUSION

Following the advancements in miniaturization, low-cost sensor technology, and development of image processing algorithms, the mission design of HYPSO-1 shows that push-broom hyperspectral imaging combined with FPGA-based onboard processing in a nanosatellite may provide ocean color data products with high spatial-spectral resolution and low data latency, this being particularly useful for monitoring rapidly changing marine environments. HYPSO-1's payload and systems design, remote sensing approach using a slew maneuver, and onboard processing, grant flexible trade-offs to be made between spatial resolution, spectral resolution, SNR, and data latency. The chosen onboard FPGA-based CCSDS123v1 lossless compression, dimensionality reduction, target detection, and classification algorithms may reduce the raw high-dimensional data size significantly without losing crucial spatial-spectral information. On the contrary to using rigorous data processing and analysis methods on the ground, such smaller yet tailored data products can be made available within minutes after first observation. This enables quicker download of relevant data that may satisfy urgent needs of operational end-users, e.g., for mitigating damage

to aquaculture caused by HABs where an early warning is critical. The lessons learned in operating HYPSO-1 will produce new iterations and potential enhancements in future planned missions such as in the hyperspectral imager design, ADCS, satellite communications architecture, and onboard image processing algorithms. After launch, the HYPSO-1 mission will determine the efficacy in quickly providing high-resolution hyperspectral data from small satellites to be used for real-time ocean color applications.

ACKNOWLEDGMENT

The authors thank Kanna Rajan at the Faculty of Engineering, University of Porto, for his substantial contribution to the HYPSO-1 mission design and his motivation toward establishing an oceanography-focused nanosatellite constellation. The authors also thank Liane S. Guild, Stephen Dunagan, and Chad Frost at NASA Ames Research Center, Raphael M. Kudela at the Ocean Sciences Department, University of California Santa Cruz, Richard P. Stumpf at the National Oceanic and Atmospheric Administration (NOAA), and Ajit Subramaniam at the Lamont-Doherty Observatory, Columbia University, for their guidance in the mission definition and systems design. The authors would also like to thank Geir Johnsen at the Department of Biology, NTNU, for his review on the requirements in ocean color remote sensing, Torbjørn Skauli at the Norwegian Defense Research Establishment (FFI) for his review on spectroscopy, Fernando Aguado-Agelet at the Department of Telecommunications Engineering, University of Vigo, and Cecilia Haskins at the Department of Mechanical Engineering, NTNU, for their input on systems engineering, Annette Stahl and Dennis Langer at the Department of Engineering Cybernetics, NTNU, for their input on image processing, Egil Eide and Gara Quintana Diaz at the Department of Electronic Systems, NTNU, for their help on radio communications, and Harald Martens, João Fortuna and Petter Rossvoll at IdleTechs for their recommendations on applicable dimensionality reduction methods for hyperspectral imagery. Finally, the authors are grateful for the participation of NanoAvionics with their continuous help and feedback throughout the project.

REFERENCES

[1] G. Johnsen *et al.*, "Optical monitoring of phytoplankton Bloom pigment signatures," in *Phytoplankton Pigments: Characterization, Chemotaxonomy and Applications in Oceanography*, S. Roy, C. A. Llewellyn, E. S. Egeland, and G. Johnsen, Eds. New York, NY, USA: Cambridge Univ. Press, Oct. 2011, ch. 14, pp. 538–606.

[2] S. Sathyendranath, *Phytoplankton Functional Types From Space*. Dartmouth, NS, Canada: IOCCG, 2014.

[3] D. Blondeau-Patissier, J. F. Gower, A. G. Dekker, S. R. Phinn, and V. E. Brando, "A review of ocean color remote sensing methods and statistical techniques for the detection, mapping and analysis of phytoplankton blooms in coastal and open oceans," *Prog. Oceanogr.*, vol. 123, pp. 123–144, Apr. 2014.

[4] T. Kutser, L. Metsamaa, N. Strömbeck, and E. Vahtmäe, "Monitoring cyanobacterial blooms by satellite remote sensing," *Estuarine, Coastal Shelf Sci.*, vol. 67, nos. 1–2, pp. 303–312, Mar. 2006.

[5] G. Johnsen, K. T. Z. Volent, and E. Sakshaug, "Time series of harmful and benign phytoplankton blooms in northwest European waters using the Seawatch buoy system," in *Monitoring Algal Blooms: New Technologies for Detecting Large-Scale Environmental Change*, M. Kahru and C. W. Brown, Eds. New York, NY, USA: Springer-Verlag, 1997, ch. 6, pp. 115–143.

[6] G. Johnsen, O. Samset, L. Granskog, and E. Sakshaug, "*In vivo* absorption characteristics in 10 classes of bloom-forming phytoplankton: Taxonomic characteristics and responses to photoadaptation by means of discriminant and HPLC analysis," *Mar. Ecol. Prog. Ser.*, vol. 105, pp. 149–157, Feb. 1994.

[7] D. A. Jessup *et al.*, "Mass stranding of marine birds caused by a surfactant-producing red tide," *PLoS One*, vol. 4, no. 2, pp. 1–8, Feb. 2009.

[8] T. D. Dickey and R. R. Bidigare, "Interdisciplinary oceanographic observations: The wave of the future," *Scientia Marina*, vol. 69, no. S1, pp. 23–42, Jun. 2005.

[9] M.-H. Forget, V. Stuart, and T. Platt, *Remote Sensing in Fisheries and Aquaculture*. Dartmouth, NS, Canada: IOCCG, 2009.

[10] C. O. Davis *et al.*, "Ocean PHILLS hyperspectral imager: Design, characterization, and calibration," *Opt. Exp.*, vol. 10, no. 4, pp. 210–221, Feb. 2002.

[11] M. R. Corson, D. R. Korwan, R. L. Lucke, W. A. Snyder, and C. O. Davis, "The hyperspectral imager for the coastal ocean (HICO) on the International Space Station," in *Proc. IEEE Int. Geosci. Remote Sens. Symp.*, Boston, MA, USA, Jul. 2008, p. 101.

[12] B.-C. Gao, M. J. Montes, C. O. Davis, and A. F. H. Goetz, "Atmospheric correction algorithms for hyperspectral remote sensing data of land and ocean," *Remote Sens. Environ.*, vol. 113, pp. S17–S24, Sep. 2009.

[13] E. J. Knight and G. Kvaran, "Landsat-8 operational land imager design, characterization and performance," *Remote Sens.*, vol. 6, no. 11, pp. 10286–10305, Oct. 2014.

[14] M. Aguirre *et al.*, "Sentinel-3—The ocean and medium-resolution land mission for GMES operational services," *ESA Bull.*, vol. 131, pp. 24–29, Aug. 2007.

[15] F. E. Muller-Karger *et al.*, "Satellite sensor requirements for monitoring essential biodiversity variables of coastal ecosystems," *Ecol. Appl.*, vol. 28, no. 3, pp. 749–760, Mar. 2018.

[16] I. Ogashawara, "The use of Sentinel-3 imagery to monitor cyanobacterial blooms," *Environments*, vol. 6, no. 6, p. 60, Jun. 2019.

[17] F. Ortenberg, "Hyperspectral sensor characteristics: Airborne, spaceborne, hand-held, and truckmounted; integration of hyperspectral data with LIDAR," in *Hyperspectral Remote Sensing of Vegetation*, P. S. Thenkabail, J. G. Lyon, and A. Huete, Eds. Boca Raton, FL, USA: CRC Press, Dec. 2011, ch. 2, pp. 39–68.

[18] J. L. Wolny *et al.*, "Current and future remote sensing of harmful algal blooms in the Chesapeake Bay to support the shellfish industry," *Frontiers Mar. Sci.*, vol. 7, p. 337, May 2020.

[19] M. Esposito and A. Z. Marchi, "In-orbit demonstration of the first hyperspectral imager for nanosatellites," in *Proc. SPIE*, vol. 11180, Jul. 2019, Art. no. 1118020.

[20] H. Dierssen, G. B. McManus, A. Chlus, D. Qiu, B.-C. Gao, and S. Lin, "Space station image captures a red tide ciliate bloom at high spectral and spatial resolution," *Proc. Nat. Acad. Sci. USA*, vol. 112, no. 48, pp. 14783–14787, Nov. 2015.

[21] L. Guanter *et al.*, "The EnMAP spaceborne imaging spectroscopy mission for Earth observation," *Remote Sens.*, vol. 7, no. 7, pp. 8830–8857, Jul. 2015.

[22] C. Mielke, N. Boesche, C. Rogass, H. Kaufmann, C. Gauert, and M. de Wit, "Spaceborne mine waste mineralogy monitoring in South Africa, applications for modern push-broom missions: Hyperion/OLI and EnMAP/Sentinel-2," *Remote Sens.*, vol. 6, no. 8, pp. 6790–6816, Jul. 2014.

[23] J. S. Pearlman, P. S. Barry, C. C. Segal, J. Shepanski, D. Beiso, and S. L. Carman, "Hyperion, a space-based imaging spectrometer," *IEEE Trans. Geosci. Remote Sens.*, vol. 41, no. 6, pp. 1160–1173, Jun. 2003.

[24] P. J. Werdell *et al.*, "The plankton, aerosol, cloud, ocean ecosystem mission: Status, science, advances," *Bull. Amer. Meteorol. Soc.*, vol. 100, no. 9, pp. 1775–1794, Sep. 2019.

[25] Y.-N. Liu *et al.*, "The advanced hyperspectral imager: Aboard China's GaoFen-5 satellite," *IEEE Geosci. Remote Sens. Mag.*, vol. 7, no. 4, pp. 23–32, Dec. 2019.

[26] D. Li, M. Wang, and J. Jiang, "China's high-resolution optical remote sensing satellites and their mapping applications," *Geo-spatial Inf. Sci.*, vol. 24, no. 1, pp. 85–94, Nov. 2020.

[27] A. Villafranca, J. Corbera, F. Martín, and J. F. Marchan, "Limitations of hyperspectral Earth observation on small satellites," *J. Small Satell.*, vol. 1, no. 1, pp. 19–29, Jan. 2012.

[28] M. N. Sweeting, "Modern small satellites-changing the economics of space," *Proc. IEEE*, vol. 106, no. 3, pp. 343–361, Mar. 2018.

[29] F. Sigernes, M. Syrjäsuo, R. Storvold, J. Fortuna, M. E. Grøtte, and T. A. Johansen, "Do it yourself hyperspectral imager for handheld to airborne operations," *Opt. Exp.*, vol. 26, no. 5, pp. 6021–6035, Mar. 2018.

[30] A. G. C. Guerra, F. Francisco, J. Villate, F. Aguado Agelet, O. Bertolami, and K. Rajan, "On small satellites for oceanography: A survey," *Acta Astronautica*, vol. 127, pp. 404–423, Oct. 2016.

[31] J. Praks *et al.*, "Miniature spectral imager in-orbit demonstration results from Aalto-1 nanosatellite mission," in *Proc. IEEE Int. Geosci. Remote Sens. Symp.*, Valencia, Spain, Jul. 2018, pp. 1986–1989.

[32] M. Guelman and F. Ortenberg, "Small satellite's role in future hyperspectral Earth observation missions," *Acta Astronautica*, vol. 64, nos. 11–12, pp. 1252–1263, Jun. 2009.

[33] A. George and C. Wilson, "Onboard processing with hybrid and reconfigurable computing on small satellites," *Proc. IEEE*, vol. 106, no. 3, pp. 458–470, Mar. 2018.

[34] S. López, T. Vladimirova, C. González, J. Resano, D. Mozos, and A. Plaza, "The promise of reconfigurable computing for hyperspectral imaging onboard systems: A review and trends," *Proc. IEEE*, vol. 101, no. 3, pp. 698–722, Mar. 2013.

[35] L. Sterpone, M. Porrmann, and J. Hagemeyer, "A novel fault tolerant and runtime reconfigurable platform for satellite payload processing," *IEEE Trans. Comput.*, vol. 62, no. 8, pp. 1508–1525, Aug. 2013.

[36] C.-I. Chang, *Hyperspectral Imaging: Techniques for Spectral Detection and Classification*. New York, NY, USA: Kluwer, 2003.

[37] M. T. Eismann, *Hyperspectral Remote Sensing*. Bellingham, WA, USA: SPIE, Apr. 2012.

[38] R. M. Kudela, S. L. Palacios, D. C. Austerberry, E. K. Accorsi, L. S. Guild, and J. Torres-Perez, "Application of hyperspectral remote sensing to cyanobacterial blooms in inland waters," *Remote Sens. Environ.*, vol. 167, pp. 196–205, Sep. 2015.

[39] K. Davidson *et al.*, "Forecasting the risk of harmful algal blooms," *Harmful Algae*, vol. 53, pp. 1–7, May 2016.

[40] C. R. McClain and G. Meister, *Mission Requirements for Future Ocean-Colour Sensors*. Dartmouth, NS, Canada: IOCCG, 2012.

[41] L. Qi, Z. Lee, C. Hu, and M. Wang, "Requirement of minimal signal-to-noise ratios of ocean color sensors and uncertainties of ocean color products," *J. Geophys. Res., Oceans*, vol. 122, no. 3, pp. 2595–2611, Mar. 2017.

[42] R. M. Kudela, S. B. Hooker, H. F. Houskeeper, and M. McPherson, "The influence of signal to noise ratio of legacy airborne and satellite sensors for simulating next-generation coastal and inland water products," *Remote Sens.*, vol. 11, no. 18, p. 2071, Sep. 2019.

[43] E. Lancheros *et al.*, "Gaps analysis and requirements specification for the evolution of Copernicus system for polar regions monitoring: Addressing the challenges in the horizon 2020–2030," *Remote Sens.*, vol. 10, no. 7, p. 1098, Jul. 2018.

[44] C. O. Davis, M. Kavanaugh, R. Letelier, W. P. Bissett, and D. Kohler, "Spatial and spectral resolution considerations for imaging coastal waters," *Proc. SPIE*, vol. 6680, Oct. 2007, Art. no. 6680P.

[45] P. Mouroulis and R. O. Green, "Review of high fidelity imaging spectrometer design for remote sensing," *Opt. Eng.*, vol. 57, no. 4, pp. 1–19, Apr. 2018.

[46] G. Vane, R. O. Green, T. G. Chrien, H. T. Enmark, E. G. Hansen, and W. M. Porter, "The airborne visible/infrared imaging spectrometer (AVIRIS)," *Remote Sens. Environ.*, vol. 44, nos. 2–3, pp. 127–143, 1993.

[47] J. E. Fowler, "Compressive pushbroom and whiskbroom sensing for hyperspectral remote-sensing imaging," in *Proc. IEEE Int. Conf. Image Process. (ICIP)*, Paris, France, Oct. 2014, pp. 684–688.

[48] D. Jervis *et al.*, "The GHGSat-D imaging spectrometer," *Atmos. Meas. Techn.*, vol. 14, no. 3, pp. 2127–2140, Mar. 2021.

[49] S. Henrot, C. Soussen, and D. Brie, "Fast positive deconvolution of hyperspectral images," *IEEE Trans. Image Process.*, vol. 22, no. 2, pp. 828–833, Feb. 2013.

[50] S. Kay, J. Hedley, and S. Lavender, "Sun glint correction of high and low spatial resolution images of aquatic scenes: A review of methods for visible and near-infrared wavelengths," *Remote Sens.*, vol. 1, no. 4, pp. 697–730, Oct. 2009.

[51] M. Lapadatu, S. Bakken, M. E. Grøtte, M. Alver, and T. A. Johansen, "Simulation tool for hyperspectral imaging from a satellite," in *Proc. 10th IEEE GRSS Workshop Hyperspectral Image Signal Process.*, Amsterdam, The Netherlands, Sep. 2019, pp. 1–5.

[52] A. Berk, P. Conforti, R. Kennett, T. Perkins, F. Hawes, and J. vanden Bosch, "MODTRAN 6: A major upgrade of the MODTRAN radiative transfer code," in *Proc. 6th IEEE GRSS Workshop Hyperspectral Image Signal Process.*, Lausanne, Switzerland, Jun. 2014, pp. 1–4.

[53] J. M. Lerner, "Imaging spectrometer fundamentals for researchers in the biosciences—A tutorial," *Cytometry A*, vol. 69A, no. 8, pp. 712–734, Aug. 2006.

[54] H. R. Gordon, "Atmospheric correction of ocean color imagery in the Earth observing system era," *J. Geophys. Res. Atmos.*, vol. 102, no. 14, pp. 17081–17106, Jul. 1997.

[55] M. Wang, "A refinement for the Rayleigh radiance computation with variation of the atmospheric pressure," *Int. J. Remote Sens.*, vol. 26, no. 24, pp. 5651–5663, Dec. 2005.

[56] W. J. Moses, J. H. Bowles, R. L. Lucke, and M. R. Corson, "Impact of signal-to-noise ratio in a hyperspectral sensor on the accuracy of biophysical parameter estimation in case II waters," *Opt. Exp.*, vol. 20, no. 4, pp. 4309–4330, Feb. 2012.

[57] T. Skauli, "Sensor noise informed representation of hyperspectral data, with benefits for image storage and processing," *Opt. Exp.*, vol. 19, no. 14, pp. 13031–13046, Jun. 2011.

[58] B. A. Franz, S. W. Bailey, P. J. Werdell, and C. R. McClain, "Sensor-independent approach to the vicarious calibration of satellite ocean color radiometry," *Appl. Opt.*, vol. 46, no. 22, pp. 5068–5082, Aug. 2007.

[59] B.-C. Gao *et al.*, "Vicarious calibrations of HICO data acquired from the International Space Station," *Appl. Opt.*, vol. 51, no. 14, pp. 2559–2567, May 2012.

[60] B.-C. Gao *et al.*, "Atmospheric correction algorithm for hyperspectral remote sensing of ocean color from space," *Appl. Opt.*, vol. 39, no. 6, pp. 887–896, Feb. 2000.

[61] D. K. Clark *et al.*, "MOBY, a radiometric buoy for performance monitoring and vicarious calibration of satellite ocean color sensors: Measurement and data analysis protocols," in *Proc. Ocean Opt. Protocols Satell. Ocean Color Sensor Validation*, Jan. 2002, pp. 3–34.

[62] A. Bucholtz, "Rayleigh-scattering calculations for the terrestrial atmosphere," *Appl. Opt.*, vol. 34, no. 15, pp. 2765–2773, May 1995.

[63] J. A. Richards and X. Jia, *Remote Sensing Digital Image Analysis: An Introduction*, 4th ed. Berlin, Germany: Springer-Verlag, Jan. 2006.

[64] A. M. Sayer, N. C. Hsu, and C. Bettenhausen, "Implications of MODIS bow-tie distortion on aerosol optical depth retrievals, and techniques for mitigation," *Atmos. Meas. Techn.*, vol. 8, no. 12, pp. 5277–5288, Dec. 2015.

[65] R. F. Stengel, *Flight Dynamics*. Princeton, NJ, USA: Princeton Univ. Press, 2004.

[66] Y. Li, C. Li, R. Zheng, X. Li, and J. Yang, "The research on image processing technology of the star tracker," in *Proc. SPIE*, vol. 9301, Nov. 2014, Art. no. 930103.

[67] T. S. Rose *et al.*, "Optical communications downlink from a 1.5U Cubesat: OCSD program," in *Proc. SPIE*, vol. 11180, Jul. 2019, Art. no. 11180J.

[68] A. Habib, Y. Han, W. Xiong, F. He, Z. Zhang, and M. Crawford, "Automated ortho-rectification of UAV-based hyperspectral data over an agricultural field using frame RGB imagery," *Remote Sens.*, vol. 8, no. 10, p. 796, Sep. 2016.

[69] *Lossless Multispectral & Hyperspectral Image Compression*, CCSDS, Washington, DC, USA, 2012.

[70] J. Fjeldtvedt, M. Orlandić, and T. A. Johansen, "An efficient real-time FPGA implementation of the CCSDS-123 compression standard for hyperspectral images," *IEEE J. Sel. Topics Appl. Earth Observ. Remote Sens.*, vol. 11, no. 10, pp. 3841–3852, Oct. 2018.

[71] J. Fjeldtvedt and M. Orlandić, "CubeDMA—Optimizing three-dimensional DMA transfers for hyperspectral imaging applications," *Microprocessors Microsyst.*, vol. 65, pp. 23–36, Mar. 2019.

[72] M. Orlandić, J. Fjeldtvedt, and T. A. Johansen, "A parallel FPGA implementation of the CCSDS-123 compression algorithm," *Remote Sens.*, vol. 11, no. 6, p. 673, Mar. 2019.

[73] S. Bakken, M. Orlandić, and T. A. Johansen, "The effect of dimensionality reduction on signature-based target detection for hyperspectral imaging," in *Proc. SPIE*, vol. 11131, Aug. 2019, Art. no. 111310L.

[74] M. B. Henriksen, J. L. Garrett, E. F. Prentice, A. Stahl, T. A. Johansen, and F. Sigernes, "Real-time corrections for a low-cost hyperspectral instrument," in *Proc. 10th IEEE GRSS Workshop Hyperspectral Image Signal Process.*, Amsterdam, The Netherlands, Sep. 2019, pp. 1–5.

[75] C. Rodarmel and J. Shan, "Principal component analysis for hyperspectral image classification," *Surv. Land Inf. Syst.*, vol. 62, no. 2, pp. 115–122, Jun. 2002.

[76] D. Fernández, C. González, D. Mozos, and S. López, "FPGA implementation of the principal component analysis algorithm for dimensionality reduction of hyperspectral images," *J. Real-Time Image Process.*, vol. 16, no. 5, pp. 1395–1406, Oct. 2019.

[77] R. Vitale, A. Zhyrova, J. F. Fortuna, O. E. de Noord, A. Ferrer, and H. Martens, "On-The-Fly processing of continuous high-dimensional data streams," *Chemometric Intell. Lab. Syst.*, vol. 161, pp. 118–129, Feb. 2017.

[78] H. Martens, J. P. Nielsen, and S. B. Engelsen, "Light scattering and light absorbance separated by extended multiplicative signal correction. Application to near-infrared transmission analysis of powder mixtures," *Anal. Chem.*, vol. 75, no. 3, pp. 394–404, Feb. 2003.

[79] D. Manolakis and G. Shaw, "Detection algorithms for hyperspectral imaging applications," *IEEE Signal Process. Mag.*, vol. 19, no. 1, pp. 29–43, Jan. 2002.

[80] D. Manolakis, "Taxonomy of detection algorithms for hyperspectral imaging applications," *Opt. Eng.*, vol. 44, no. 6, Jun. 2005, Art. no. 066403.

[81] Đ. Bošković, M. Orlandić, and T. A. Johansen, "A reconfigurable multimode implementation of hyperspectral target detection algorithms," *Microprocessors Microsyst.*, vol. 78, Oct. 2020, Art. no. 103258.

[82] Đ. Bošković, M. Orlandić, S. Bakken, and T. A. Johansen, "HW/SW implementation of hyperspectral target detection algorithm," in *Proc. 8th Medit. Conf. Embedded Comput. (MECO)*, Budva, Montenegro, Jun. 2019, pp. 1–6.

[83] A. Alcolea, M. E. Paoletti, J. M. Haut, J. Resano, and A. Plaza, "Inference in supervised spectral classifiers for on-board hyperspectral imaging: An overview," *Remote Sens.*, vol. 12, no. 3, p. 534, Feb. 2020.

[84] Y. Zhao, Y. Yuan, and Q. Wang, "Fast spectral clustering for unsupervised hyperspectral image classification," *Remote Sens.*, vol. 11, no. 4, p. 399, Feb. 2019.

[85] R. Wang, F. Nie, and W. Yu, "Fast spectral clustering with anchor graph for large hyperspectral images," *IEEE Geosci. Remote Sens. Lett.*, vol. 14, no. 11, pp. 2003–2007, Nov. 2017.

[86] M. Ismail and M. Orlandić, "Segment-based clustering of hyperspectral images using tree-based data partitioning structures," *Algorithms*, vol. 13, no. 12, p. 330, Dec. 2020.

[87] T. Opsahl, T. V. Haavardsholm, and I. Winjum, "Real-time georeferencing for an airborne hyperspectral imaging system," in *Proc. SPIE*, vol. 8048, May 2011, Art. no. 80480S.

[88] D. Schläpfer and R. Richter, "Geo-atmospheric processing of airborne imaging spectrometry data. Part 1: Parametric orthorectification," *Int. J. Remote Sens.*, vol. 23, no. 13, pp. 2609–2630, Jan. 2002.

[89] S. C. Park, M. K. Park, and M. G. Kang, "Super-resolution image reconstruction: A technical overview," *IEEE Signal Process. Mag.*, vol. 20, no. 3, pp. 21–36, May 2003.

[90] H. Stark and P. Oskoui, "High-resolution image recovery from image-plane arrays, using convex projections," *J. Opt. Soc. Amer. A, Opt. Image Sci.*, vol. 6, no. 11, pp. 1715–1726, Nov. 1989.

[91] S. Farsiu, M. Robinson, M. Elad, and P. Milanfar, "Fast and robust multiframe super resolution," *IEEE Trans. Image Process.*, vol. 13, no. 10, pp. 1327–1344, Oct. 2004.

[92] J. L. Garrett, D. Langer, K. Avagian, and A. Stahl, "Accuracy of super-resolution for hyperspectral ocean observations," in *Proc. OCEANS*, Marseille, France, Jun. 2019, pp. 1–5.

[93] L. Clarisse, M. Van Damme, C. Clerbaux, and P.-F. Coheur, "Tracking down global NH_3 point sources with wind-adjusted superresolution," *Atmos. Meas. Techn.*, vol. 12, no. 10, pp. 5457–5473, Oct. 2019.

[94] S. Baker and T. Kanade, "Limits on super-resolution and how to break them," *IEEE Trans. Pattern Anal. Mach. Intell.*, vol. 24, no. 9, pp. 1167–1183, Sep. 2002.

[95] T. Köhler, M. Bätz, F. Naderi, A. Kaup, A. Maier, and C. Riess, "Toward bridging the simulated-to-real gap: Benchmarking super-resolution on real data," *IEEE Trans. Pattern Anal. Mach. Intell.*, vol. 42, no. 11, pp. 2944–2959, Nov. 2020.

[96] J. Yang, J. Wright, T. S. Huang, and Y. Ma, "Image super-resolution via sparse representation," *IEEE Trans. Image Process.*, vol. 19, no. 11, pp. 2861–2873, Nov. 2010.

[97] J. Kim, J. K. Lee, and K. M. Lee, "Accurate image super-resolution using very deep convolutional networks," in *Proc. IEEE Conf. Comput. Vis. Pattern Recognit.*, Las Vegas, NV, USA, Jun. 2016, pp. 1646–1654.

[98] S. Anwar, S. Khan, and N. Barnes, "A deep journey into super-resolution: A survey," *ACM Comput. Surv.*, vol. 53, no. 3, pp. 1–34, Jul. 2020.

[99] C. Lanaras, E. Baltsavias, and K. Schindler, "Hyperspectral super-resolution by coupled spectral unmixing," in *Proc. IEEE Int. Conf. Comput. Vis. (ICCV)*, Santiago, Chile, Dec. 2015, pp. 3586–3594.

[100] N. Yokoya, C. Grohnfeldt, and J. Chanussot, "Hyperspectral and multispectral data fusion: A comparative review of the recent literature," *IEEE Geosci. Remote Sens. Mag.*, vol. 5, no. 2, pp. 29–56, Jun. 2017.

[101] T. Akgun, Y. Altunbasak, and R. M. Mersereau, "Super-resolution reconstruction of hyperspectral images," *IEEE Trans. Image Process.*, vol. 14, no. 11, pp. 1860–1875, Nov. 2005.

[102] K. Avagian and M. Orlandić, "An efficient FPGA implementation of Richardson-Lucy deconvolution algorithm for hyperspectral images," *Electronics*, vol. 10, no. 4, p. 504, Feb. 2021.

[103] K. Avagian, M. Orlandić, and T. A. Johansen, "An FPGA-oriented HW/SW codesign of Lucy-Richardson deconvolution algorithm for hyperspectral images," in *Proc. 8th Medit. Conf. Embedded Comput. (MECO)*, Budva, Montenegro, Jun. 2019, pp. 1–6.

[104] R. S. Fraser, S. Mattoo, E.-N. Yeh, and C. R. McClain, "Algorithm for atmospheric and glint corrections of satellite measurements of ocean pigment," *J. Geophys. Res. Atmos.*, vol. 102, pp. 17107–17118, Jul. 1997.

[105] T. Schroeder, I. Behnert, M. Schaale, J. Fischer, and R. Doerffer, "Atmospheric correction algorithm for MERIS above case-2 waters," *Int. J. Remote Sens.*, vol. 28, no. 7, pp. 1469–1486, Apr. 2007.

[106] M. Wang, *Atmospheric Correction for Remotely-Sensed Ocean-Colour Products*. Dartmouth, NS, Canada: IOCCG, 2010.

[107] B. Gao and R. Li, "Spectral calibrations of HICO data using atmospheric bands and radiance adjustment based on HICO and MODIS data comparisons," in *Proc. IEEE Int. Geosci. Remote Sens. Symp.*, Honolulu, HI, USA, Jul. 2010, pp. 4260–4263.

[108] K. Stamnes *et al.*, "Progress in forward-inverse modeling based on radiative transfer tools for coupled atmosphere-snow/ice-ocean systems: A review and description of the AccuRT model," *Appl. Sci.*, vol. 8, no. 12, p. 2682, Dec.2018.

[109] O. M. Borge, S. Bakken, and T. A. Johansen, "Atmospheric correction of hyperspectral data over coastal waters based on machine learning models," in *Proc. 11th IEEE GRSS Workshop Hyperspectral Image Signal Process.*, Amsterdam, The Netherlands, Mar. 2021, pp. 1–5.

Mariusz E. Grøtte (Member, IEEE) received the M.Sc. degree in aerospace engineering from the Georgia Institute of Technology, Atlanta, GA, USA, in 2015, and the B.Eng. (Hons.) degree in aerospace engineering from The University of Manchester, Manchester, U.K., in 2013. He is pursuing the Ph.D. degree with the Department of Engineering Cybernetics, Norwegian University of Science and Technology (NTNU), Trondheim, Norway.

He was a Visiting Researcher with the NASA Ames Research Center, Moffett Field, CA, USA, from 2018 to 2019. His research focuses on small satellite remote sensing, nonlinear control, and optimal control.

Roger Birkeland (Member, IEEE) received the M.Sc. degree in electronic engineering and the Ph.D. degree in satellite communications from the Norwegian University of Science and Technology (NTNU), Trondheim, Norway, in 2007 and 2019, respectively.

He is a Post-Doctoral Researcher with the Department of Electronic Systems, NTNU. He is researching small satellite systems and heterogeneous communication systems for remote areas.

Evelyn Honoré-Livermore (Graduate Student Member, IEEE) received the M.Sc. degree in electronic engineering from the Norwegian University of Science and Technology (NTNU), Trondheim, Norway, in 2012, and the M.B.A. degree from Yonsei University, Seoul, South Korea, in 2017. She is pursuing the Ph.D. degree with the Department of Electronic Systems, NTNU.

She is researching systems engineering and project management methods for academic research projects. She is also the Project Manager of the HYPSO Project.

Sivert Bakken (Member, IEEE) is pursuing the Ph.D. degree with the Department of Engineering Cybernetics, Norwegian University of Science and Technology (NTNU), Trondheim, Norway.

He is researching on how to utilize small satellites with hyperspectral imager as intelligent agents in coordinated missions involving autonomous agents, and developing methods to advance the usefulness of ocean color data. He is responsible for the software development on HYPSO satellite(s).

Joseph L. Garrett (Member, IEEE) received the B.Sc. degree in physics and mathematics from The Ohio State University, Columbus, OH, USA, in 2011, and the Ph.D. degree in physics from the University of Maryland, College Park, MD, USA, in 2017.

He studies hyperspectral imaging and image processing from satellites and drones as a Postdoctoral Researcher with the Norwegian University of Science and Technology (NTNU), Trondheim, Norway.

Elizabeth F. Prentice (Member, IEEE) is pursuing the Ph.D. degree with the Department of Engineering Cybernetics, Norwegian University of Science and Technology (NTNU), Trondheim, Norway.

She is researching optical remote sensing and mechanical integration for small satellites and robotic agents. She is responsible for hardware development on the HYPSO mission at NTNU.

Fred Sigernes (Member, IEEE) is a Full Professor of optics and atmospheric research with the University Centre in Svalbard (UNIS), Longyearbyen, Norway, and the Head of the Kjell Henriksen Observatory (KHO), Breinosa, Svalbard and Jan Mayen. He is a Team Leader for the ground-based activity with the Birkeland Center for Space Science (BCSS), University of Bergen, Bergen, Norway, and a Professor II at AMOS, Norwegian University of Science and Technology (NTNU), Trondheim, Norway. His main expertise is spectroscopy with focus on aurora.

Milica Orlandić (Member, IEEE) received the B.Sc. and M.Sc. degrees in electrical engineering from the University of Montenegro, Podgorica, Montenegro, in 2007 and 2009, respectively, and the Ph.D. degree in electronics from the Norwegian University of Science and Technology (NTNU), Trondheim, Norway, in 2015.

She holds the position of Associate Professor of electronic systems engineering at NTNU. Her research interests include digital hardware design of hyperspectral imaging, satellite onboard processing systems, and high-performance reconfigurable systems.

J. Tommy Gravdahl (Senior Member, IEEE) received the Siv.Ing. and Dr.Ing. degrees in engineering cybernetics from the Norwegian University of Science and Technology (NTNU), Trondheim, Norway, in 1994 and 1998, respectively.

He was appointed as an Associate Professor and a Professor with the Department of Engineering Cybernetics, NTNU, in 2001 and 2005, respectively. He was the Head of the Department of Engineering Cybernetics from 2008 to 2009. He has supervised the graduation of 140 M.Sc. and 14 Ph.D. candidates. He has published five books and more than 250 articles in international conferences and journals. His research interests include mathematical modeling and nonlinear control in general, in particular applied to turbomachinery, marine vehicles, spacecraft, robots, and high-precision mechatronic systems.

Dr. Gravdahl received the IEEE Transactions on Control Systems Technology Outstanding Paper Award in 2000 and 2017. He is a Senior Editor of the *Mechatronics* (IFAC journal) and an Associate Editor of the IEEE TRANSACTIONS ON CONTROL SYSTEMS TECHNOLOGY.

Tor A. Johansen (Senior Member, IEEE) received the M.Sc. and Ph.D. degrees in electrical and computer engineering from the Norwegian University of Science and Technology (NTNU), Trondheim, Norway, in 1989 and 1994, respectively.

From 1995 to 1997, he worked at SINTEF as a Researcher before he was appointed Associated Professor with the NTNU, in 1997, and a Professor in 2001. He has published several hundred articles in the areas of control, estimation and optimization with applications in the marine, aerospace, automotive, biomedical and process industries. In 2002, he cofounded the company Marine Cybernetics AS, Trondheim, where he was a Vice President until 2008.

Dr. Johansen received the 2006 Arch T. Colwell Merit Award of the SAE and is a Principal Researcher within the Center of Excellence on Autonomous Marine Operations and Systems (NTNU-AMOS), Trondheim, and the Director of the Unmanned Aerial Vehicle Laboratory at NTNU and the SmallSat Laboratory at NTNU. He recently cofounded the spin-off companies Scout Drone Inspection, UBIQ Aerospace, Zeabuz and SentiSystems.